Rotary atomization of Newtonian and viscoelastic liquids

Rotary atomization of Newtonian and viscoelastic liquids

Bavand Keshavarz,[1,*] Eric C. Houze,[2] John R. Moore,[2]
Michael R. Koerner,[2] and Gareth H. McKinley[1]

[1]*Hatsopoulos Microfluids Laboratory, Department of Mechanical Engineering, Massachusetts Institute of Technology, Cambridge, Massachusetts 02139, USA*

[2]*Axalta Coating Systems, Two Commerce Square, 2001 Market Street, Suite 3600, Philadelphia, Pennsylvania 19103, USA*

(Received 25 September 2019; accepted 14 January 2020; published 5 March 2020)

We study the dynamics of fragmentation for Newtonian and viscoelastic liquids in rotary atomization. In this common industrial process centripetal acceleration destabilizes the liquid torus that forms at the rim of a spinning cup or disk due to the Rayleigh-Taylor instability. The resulting ligaments leave the liquid torus with a remarkably repeatable spacing that scales inversely with the rotation rate. The fluid filaments then follow a well-defined geometrical path-line that is described by the involute of a circle. Knowing the geometry of this phenomenon we derive the detailed kinematics of this process and compare it with the experimental observations. We show that the ligaments elongate tangentially along the involute of the circle and thin radially as they separate from the cup. We use these kinematic conditions to develop an expression for the spatial variation of the filament deformation rate and show that it decays away from the spinning cup. Once the ligaments are sufficiently far from the cup, they are not stretched sufficiently fast to overcome the critical rate of capillary thinning and consequently undergo capillary-driven breakup forming droplets. We couple these kinematic considerations with the known properties of several Newtonian and viscoelastic test liquids to develop a quantitative understanding of this commercially important fragmentation process that can be compared in detail with experimental observations. We also investigate the resulting droplet size distributions and observe that the appearance of satellite droplets during the pinch-off process lead to the emergence of bidisperse droplet size distributions. These binary distributions are well described by the superposition of two separate Γ distributions that capture the physics of the disintegration process for the main and satellite droplets, respectively. Furthermore, as we consider more viscous Newtonian liquids or weakly viscoelastic test fluids, we show that changes in the liquid viscosity or viscoelasticity have a negligible effect on the *average* droplet size. However, incorporation of viscous/viscoelastic effects delays the thinning dynamics in the ligaments and thus results in broader *droplet size distributions*. The ratio of the primary to satellite droplet size increases monotonically with both viscosity and viscoelasticity. We develop a simple physical model that rationalizes the observed experimental trends and provides us a better understanding of the principal dynamical features of rotary fragmentation for both Newtonian and weakly viscoelastic liquids.

DOI: 10.1103/PhysRevFluids.5.033601

I. INTRODUCTION

Animals drying their wet fur by rapidly shaking their body [1,2] and automated rotary atomization in paint coating [3] are just two examples in which centripetal acceleration is used to

*bavand@mit.edu

disintegrate liquid films into a wide distribution of smaller fragments. The interest in this type of atomization goes back to the pioneering studies on different combustion and spray drying designs. Peter Bär [4] (son of the founder of the Julius Bär private Swiss banking group) was the first who systematically studied a design for a "centripetal atomizer." At the time of invention, this simple design was used for a new type of spray-dryer and consisted of a tube that delivered the fluid of interest into a rotating cup. More recent designs follow more or less the same basic principles [5–7].

With increasing industrial interest, researchers began to study this type of atomization in more detail. Hinze and Milborn [8] performed a series of experiments with different Newtonian liquids and provided several semiempirical correlations for the performance of rotary atomizers. Early high-speed photographic visualization by Hinze and Milborn also showed that, for certain ranges of rotation speeds and fluid delivery rates, evenly spaced ligaments emerge on the edge of the spinning cup that is used as the atomizer.

Narrower size distributions and well-defined geometrical spiral fluid ligaments were found to be the main advantages of this type of atomization as compared to air-assisted atomization [9–11]. These features have made rotary fragmentation one of the most frequently used atomization methods in industries such as metal particle production [12], ceramic spray drying [13], agricultural spraying [14], spray drying/cooling [13,15,16], and paint coating for the automotive industry [17–19].

By varying the flow rate and the centripetal acceleration, researchers have observed several different regimes of fragmentation for Newtonian liquids [20–22]. There have been several attempts at quantifying the transition criteria separating these different regimes [20,21,23,24]. Also, several semiempirical correlations have been suggested for the variation in average droplet size with rotation rate, feed rate and fluid properties [11,21,25–27]. Some other recent studies have taken numerical, theoretical and experimental approaches to characterize the mean droplet sizes in sprays produced by spinning disk atomizers [28,29]. However, even for Newtonian liquids, a detailed kinematic analysis and physical model for the final droplet size distributions developed in this type of fragmentation are still missing.

Despite the inherent advantages offered by rotary atomization and its various applications with a range of industrially important fluids such as paints, there is also a paucity of fundamental knowledge about the roles of fluid rheology in this process. In this paper, we study the effects of varying fluid viscosity and fluid viscoelasticity by performing rotary atomization tests on different Newtonian and dilute polymer solutions.

II. EXPERIMENTAL SETUP

We have designed a rotary atomization setup which is very similar to the one described by Fraser *et al.* [9,10]. As shown in Fig. 1, the fluid is delivered to the rotating cup through a swivel joint at the back of the spinning cup. The fluid is then accelerated outwards to the rim of the conical cup surface. A high-speed camera (Phantom-Miro series) is mounted in front of the spinning cup recording the fragmentation process at high spatial (1400×800 pixels) and temporal (4000 fps recording speed) resolution. To spin the cup at the desired rate of rotation, a mechanical assembly was designed and fabricated in the MIT machine shop. Figures 1(a) and 1(b) show CAD drawings of the design and the final prototype is shown in Fig. 1(c). A stepper motor precisely controls the rotation of the cup through a timing belt pulley, the liquid is delivered through the swivel joint that allows the transfer of liquid from a fixed tube to the rotating cup. A precision syringe pump (Harvard PHD ULTRA) is used to feed the liquid into the cup at a constant volumetric flow rate spanning the range $0.1 \leqslant Q \leqslant 200$ ml/min. The entire setup is then mounted and fixed in a transparent glass box minimizing the spread of drop fragments ('misting') while remaining optically accessible for high speed imaging purposes.

The high speed rotary motion of the cup and the liquid drops/ligaments can lead to optically blurred images, especially at higher values of the rotation rate which typically span 3 rad/s $\leqslant \omega \leqslant$ 346 rad/s in our studies. To avoid this, we chose relatively small values of exposure times in our high-speed recordings ($\sim$20 μs). Using a back-lighting technique, we are able to provide ample

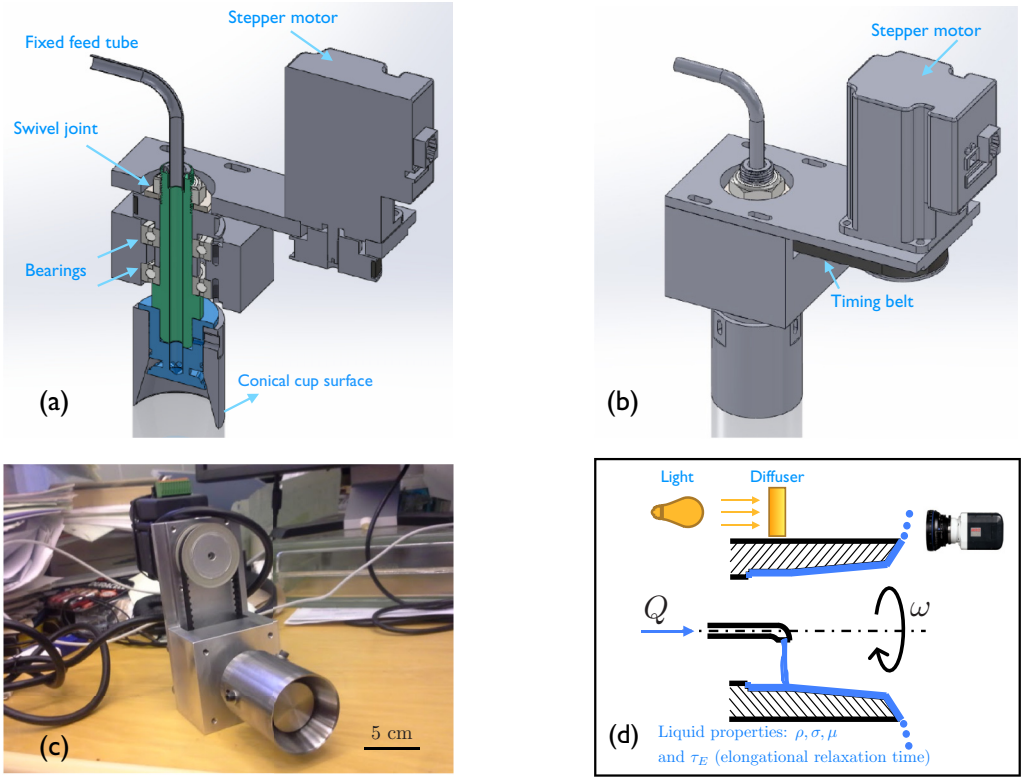

FIG. 1. (a, b) Solidworks CAD drawings of the initial design for the rotary atomizer. (c) The final assembled prototype. (d) Schematic diagram of the visualization setup. A cup with outer diameter $D = 2R = 3.18$ cm, rotating at an angular speed ω, is supplied with a liquid at a volumetric flow rate Q. As a result of centrifugal forces, the liquid is pushed axially and radially outwards to the rim of the cup and forms a toroidal ridge of fluid which then disintegrates into smaller fragments. A high-speed camera (Phantom-Miro) is used to visualize the fragmentation process.

illumination for recordings at these low values of exposure time. A bright halogen lamp (250 W) with an optical diffuser (a diffusive plastic filter) were fixed behind the rim of the cup and the shadow of the fragmentation event was recorded. Figure 1(d) shows the viewing angle of the high-speed camera and Fig. 2 shows a typical frame from the recorded movie which shows the atomization of silicone oil ($\nu = 100$ cSt) at $\omega = 62.8$ rad/s. The outer profile of each filament/drop is seen as a dark shadow with high contrast compared to the uniform grayscale background. The bright inner core that can be detected in the filaments and drops is due to the well-known lensing effect that each cylindrical/spherical transparent object generates. All the important features of the phenomena, such as sizes and numbers of ligaments can readily be captured by simple image-processing schemes in Matlab or ImageJ. The fact that the entire fragmentation event happens in the fixed plane formed by the edge of the cup is extremely helpful in imaging and the post-processing analysis of the data.

III. TEST FLUIDS

We prepared several different Newtonian liquids for our study and used certain subsets of them in different tests. Five different silicone oils were purchased from Gelest and a low viscosity aqueous Newtonian fluid was also prepared by mixing ethanol and water with a 90%–10% weight ratio. The properties of these Newtonian liquids are tabulated in Table I.

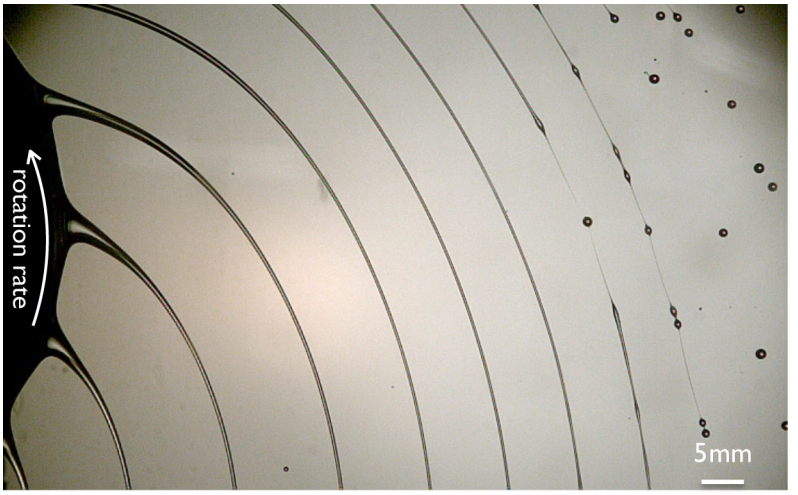

FIG. 2. Silicone oil ($\nu = 100$ cSt) flows into the rotating cup ($\omega = 62.8$ rad s^{-1}) at a constant volumetric flow rate ($Q = 60$ ml/min). The liquid forms a thin torus-like film at the rim of the spinning cup which then becomes unstable due to centripetal acceleration and forms a series of evenly-spaced continuously elongating liquid ligaments. These ligaments form a periodic spiral-like pattern that is quantified in the text below. Capillary forces become increasingly strong in the thinning filaments and ultimately make the individual ligaments unstable. Consequently, each liquid thread breaks into a series of small droplets.

To study the effect of viscoelasticity on the rotary fragmentation process, we also dissolved a flexible high molecular weight homopolymer, poly(ethylene oxide) (PEO), in the ethanol-water mixture and prepared three dilute polymer solutions. Two of the viscoelastic solutions were formulated from a PEO with mass average molecular weight $M_w = 300$K. They were dissolved at concentrations of $c = 0.01\%$ and $c = 0.05\%$ wt. into the solvent. Another viscoelastic solution was also made with a high molecular weight PEO ($M_w = 1000$K) at a concentration of $c = 0.01\%$ wt. concentration. The properties of the viscoelastic test fluids are tabulated in Table II. For these solutions the zero-shear-rate viscosity is almost constant and close to the corresponding value of the solvent but, as discussed in [30,31], the elongational viscosity of dilute polymer solutions can be raised dramatically at sufficiently high elongational rates. Measurements of the elongational relaxation times τ_E were carried out using the ROJER (Rayleigh-Ohnesorge-Jetting-Extensional-Rheometer) technique [31] and the measured values are also given in Table II.

TABLE I. Properties of the Newtonian test fluids. Five silicone oils with different viscosities ($\nu =$ 7, 20, 50, 100, and 1000 cSt) were used in our tests. An ethanol-water mixture (90%–10% wt. $\eta_s = 1.0$ mPa s) was also prepared as the Newtonian solvent used in aqueous polymer solutions described later. Values of the Ohnesorge number ($\mathrm{Oh}_R \equiv \mu/\sqrt{\rho\sigma R}$) for each fluid are also given.

Liquid	μ[mPa s]	σ[mN m]	ρ[kg/m^3]	Oh_R
Silicone oil (7 cSt)	6.44	18	920	0.011
Silicone oil (20 cSt)	19	20	950	0.033
Silicone oil (50 cSt)	48	22	960	0.082
Silicone oil (100 cSt)	96	22	960	0.166
Silicone oil (1000 cSt)	970	22	970	1.667
Ethanol-water (90%–10%)	1	23	825	0.001

TABLE II. Properties of the viscoelastic test fluids. Three different dilute polymer solutions were prepared by dissolving small amounts of PEO [poly(ethylene oxide)] in the Newtonian solvent (ethanol-water mixture). Definitions of the Deborah number (De_R), and Ohnesorge number (Oh_R), are described in the text.

Liquid	M_w	c(wt.)	c/c^*	η_0[mPa s]	σ[mN m]	$\tau_E[\mu s]$	De_R	Oh_R
1M–0.01%	1000K	0.01%	0.07	1.08	23	900	0.005	0.001
300K–0.05%	300K	0.05%	0.18	1.16	23	109	0.0006	0.001
300K–0.01%	300K	0.01%	0.04	1.04	23	68	0.0004	0.001

IV. DIMENSIONLESS OPERATING MAP

To help understand the underlying physics of the rotary fragmentation, we first consider the different timescales that are involved in this complex unsteady free-surface phenomenon. A Newtonian liquid with density ρ, viscosity μ and surface tension σ is delivered, at a volumetric rate Q, into a cup of size $D = 2R$ that is rotating at a steady rotation rate ω. Based on these physical variables, four timescales are involved in these atomization phenomena: the rotation timescale $1/\omega$, the convective timescale R^3/Q, the inertia-capillary or Rayleigh timescale $\tau_R \equiv \sqrt{\rho R^3/\sigma}$ and a viscous timescale $\mu R/\sigma$. From these four timescales, we can naturally construct three dimensionless groups by comparing the capillary timescale with the each of the remaining timescales:

$$\mathrm{We}_{\mathrm{rotation}} \equiv \left(\frac{\sqrt{\rho R^3/\sigma}}{1/\omega}\right)^2 = \frac{\rho R^3\omega^2}{\sigma}, \tag{1}$$

$$\mathrm{We}_{\mathrm{convection}} \equiv \left(\frac{\sqrt{\rho R^3/\sigma}}{R^3/Q}\right)^2 = \frac{\rho Q^2}{R^3\sigma}, \tag{2}$$

$$\mathrm{Oh}_R \equiv \left(\frac{\sqrt{\rho R^3/\sigma}}{\mu R/\sigma}\right)^{-1} = \frac{\mu}{\sqrt{\rho R\sigma}}. \tag{3}$$

Two distinct Weber numbers can be constructed based on the momentum of the fluid arising from the cup rotation (ω) or the convective feed supply (Q). Each of these Weber groups compares a ratio of the inertially generated stresses in the flow to the capillary forces during breakup at the air/liquid interface. In this paper we use the simplified notation We to refer to the rotational Weber number $\mathrm{We}_{\mathrm{rotation}}$. The convective Weber number can always be found as the product $\mathrm{We}[(Q/R^3)/\omega]^2$. The last dimensionless group that emerges from this analysis is independent of rotational and convective effects and is the familiar Ohnesorge number that describes the ratio of viscous to inertia-capillary stresses [32].

As mentioned, many liquids of interest in rotary atomization processes are complex fluids such as paint or inks, which are often weakly viscoelastic in character. These complex fluids have an underlying microstructure that can deform and resist the strong elongational kinematics that are induced by the pinch-off processes encountered in late stages of the rotary atomization. Comparing the elongational relaxation timescale τ_E of a viscoelastic liquid to the inertia-capillary timescale τ_R gives rise to a new dimensionless number:

$$De_R \equiv \frac{\tau_E}{\tau_R} = \frac{\tau_E}{\sqrt{\rho R^3/\sigma}}. \tag{4}$$

This group can be viewed as an intrinsic Deborah number for this atomization process [33]. Hinze and Milborn [8] were some of the first researchers to use the dimensionless numbers defined in Eqs. (1)–(3) in their study of the rotary atomization for Newtonian liquids (a more recent study has been performed by Truscott and coworkers [24]). In their studies they found that by increasing either the rotation rate of the cup, or the flow rate of the supplied fluid, three separate regimes

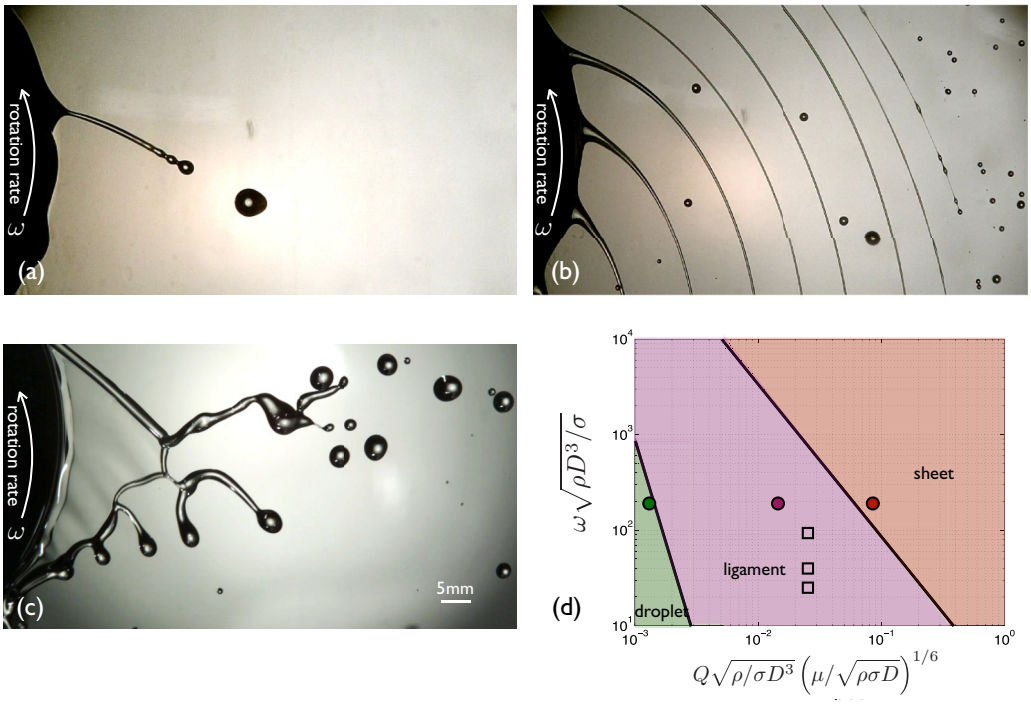

FIG. 3. Visualization of the rotary fragmentation process showing the formation of (a) single drops, (b) ligaments, and (c) a fluid sheet for a Newtonian silicone oil ($\nu = 50$ cSt) as the flow rate increases from (a) to (c). The cup of diameter $D = 2R = 3.18$ cm is rotating at the same rate for the three images ($\omega = 165$ rad/s) and the corresponding dimensionless groups based on the cup diameter are $\Pi_1 \equiv \omega\sqrt{\rho D^3/\sigma}$ and $\Pi_2 \equiv (Q)\sqrt{\rho/(\sigma D^3)}(\mu/\sqrt{\rho\sigma D})^{1/6}$. The values for each image are (a) $\{\Pi_1 = 1.95 \times 10^2, \Pi_2 = 1.64 \times 10^{-3}\}$, (b) $\{\Pi_1 = 1.95 \times 10^2, \Pi_2 = 1.64 \times 10^{-2}\}$, and (c) $\{\Pi_1 = 1.95 \times 10^2, \Pi_2 = 9.83 \times 10^{-2}\}$. (d) The proposed dimensionless map of rotary atomization showing the boundaries given by Hinze and Milborn [8]. The filled circles correspond to images (a), (b), and (c) in Fig. 3 and the open squares correspond to the images (a), (b), and (c) in Fig. 5. The dividing lines distinguishing the three possible morphologies (drop, ligament, and film generation) are given in the text [Eq. (5)].

emerge and they represented these regimes in a dimensionless parameter space corresponding to the values of two closely related dimensionless product groups $\Pi_1 = \omega\sqrt{\rho D^3/\sigma} = \sqrt{8\mathrm{We}}$ and $\Pi_2 = Q\sqrt{\rho/D^3\sigma}(\mu/\sqrt{\rho D\sigma})^{1/6} = \sqrt{\mathrm{We}_{\mathrm{convection}}/8}(\mathrm{Oh}/\sqrt{2})^{1/6}$. Figure 3 provides a summary of these distinct regimes:

(a) At low rotation/flow rates, single drops are intermittently formed at the edge of the cup ("*single drop formation*"). Due to the centripetal acceleration of the spinning liquid ridge these drops finally grow large enough to pinch off and separate from the cup.

(b) At larger values of the rotation rate and/or flow rate, many evenly-spaced ligaments appear on the cup and each ligament follows a repeatable spiral-like geometry in space ("*ligament formation*"). Due to the increasing importance of capillary forces as the ligament stretches and thins, each thread finally breaks up into a sequence of droplets that is relatively monodisperse in size thanks to the repeatable and well-organized spiral geometry of the individual ligaments.

(c) At large enough rotation/flow rates a continuous liquid sheet emerges from the edge of the cup ("*film formation*"). This liquid sheet initially rotates with the cup and is ultimately destabilized due to the inertia of its motion in the air through Kelvin-Helmholtz instability [11]. The sheet forms an unstable rim that breaks into droplets with a wide range of sizes.

Hinze and Milborn [8] recognized that the regime corresponding to ligament formation is the best regime for the performance of rotary atomization in terms of monodispersity in the final droplet size distributions. To find the operating criteria that differentiate ligament formation from the other two regimes, they atomized a wide variety of different liquids with different cup sizes. Following the principles of dimensional analysis, they found that the following semiempirical dimensionless criteria can describe the drop-to-ligament and ligament-to-film transitions, respectively:

$$\left[\omega\sqrt{\frac{\rho D^3}{\sigma}}\right]^{0.25} Q\sqrt{\frac{\rho}{\sigma D^3}}(\mu/\sqrt{\rho\sigma D})^{1/6} = \Pi_1^{0.25}\Pi_2 = 2.88\times 10^{-3}: \text{ drop-ligament},$$

$$\left[\omega\sqrt{\frac{\rho D^3}{\sigma}}\right]^{0.6} Q\sqrt{\frac{\rho}{\sigma D^3}}(\mu/\sqrt{\rho\sigma D})^{1/6} = \Pi_1^{0.6}\Pi_2 = 0.442\text{: ligament-film.} \tag{5}$$

These criteria are replotted in Fig. 3(d) to construct a dimensionless operational map for the three different regimes: drop formation (shaded in green), ligament formation (shaded in magenta) and film formation (shaded in red).

V. ROTARY ATOMIZATION OF NEWTONIAN LIQUIDS

As we have noted above, the optimal regime for continuous reproducible operation of rotary atomization is the ligament formation regime. Thus, for the rest of this paper, we focus principally on an analysis of the kinematics in this regime, first for Newtonian fluids and then for weakly viscoelastic fluids.

A. Average droplet sizes

Several previous studies in the literature have reported empirical correlations for the average droplet diameter $\langle d\rangle$ measured in rotary atomization of Newtonian liquids as the fluid properties (ρ, μ, σ) and operating conditions are varied [11,21,25–27]. Dombrowski and Lloyd [11] report a summary of the power-law exponents that are suggested in the literature. They show that, due to the empirical nature of most studies, there are discrepancies between the suggested correlations. It should also be emphasized that the dimensional analysis outlined above can not really add any further certainty to any of the proposed correlations. We thus aim to understand the phenomena in a more detailed manner and provide a physical model for the prediction of average droplet size to be expected.

B. Parameter study

We first measured average droplet sizes $\langle d\rangle$ at a series of different rotation and flow rates for several of the lowest viscosity Newtonian fluids and the results are plotted in Fig. 4.

The results clearly exhibit power law dependencies between the average droplet diameters and the applied rotation/flow rates. The measured average droplet size decreases strongly with increasing the rotation rate as $\langle d\rangle \sim \omega^{-0.88}$ and shows a weaker increase in average droplet size as the volumetric flow rate of the feedstock is increased $\langle d\rangle \sim Q^{0.30}$. Although these power law exponents are similar to the reported values in the literature [11], they still fail to give us a clear physical image of the rotary atomization phenomenon. To understand what physical phenomena drive the observed correlations for the ligament formation regime, we start by seeking to understand the mechanism of ligament generation and focus on the kinematics of the flow in this regime.

C. Formation of ligaments

It is clear from Fig. 4 that viscous effects do not play a role in controlling the mean droplet size (at least for low viscosity fluids with $\mathrm{Oh}_R << 1$). It is the centripetal acceleration $\omega^2 R$ that

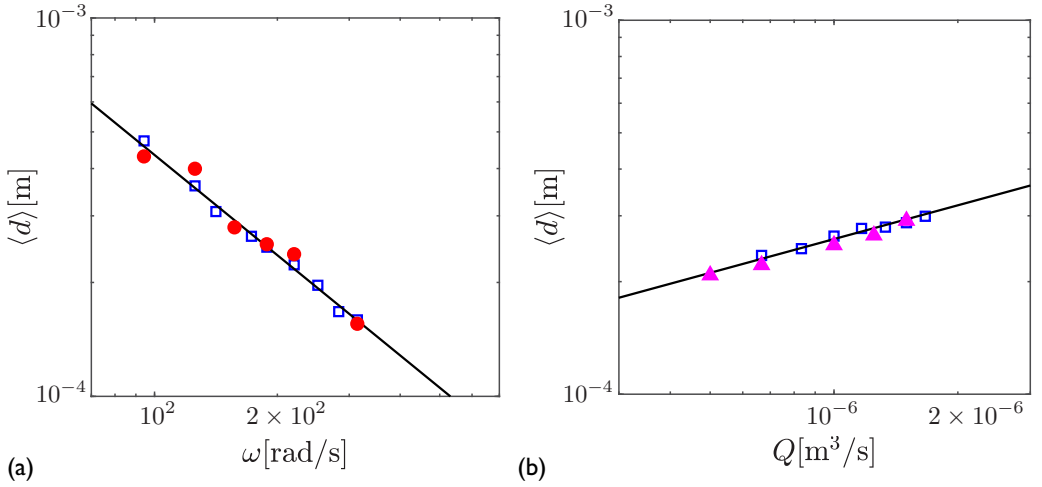

FIG. 4. Measured values of the average droplet diameter for the ethanol-water (90%–10% wt.) mixture (□), the silicone oil with $\nu = 50$ cSt (●), and silicone oil with $\nu = 7$ cSt (▲). Dependency of the average droplet diameter $\langle d \rangle$ on: (a) the rotation rate of the cup ω at a fixed value of volumetric flow rate $Q = 60$ ml/min and (b) the corresponding variation of droplet size with increasing volumetric flow rate Q at a fixed rotation rate $\omega = 172.7$ rad/s.

provides the driving force for this fragmentation process. Inside the cup, liquid elements are pushed radially and axially outwards and finally reach the rim of the cup. As the liquid accumulates, a liquid torus is formed around the rim that has a tendency to preserve its toroidal shape due to the action of surface tension. However, if a small perturbation in the size of this torus occurs, then fluid elements further from the axis of rotation feel higher accelerations that overcome the resisting capillary pressure and the torus becomes unstable forming elongated fingers that turn into ligaments when they are stretched. This mechanism is identical to the well-known Rayleigh-Taylor instability [34–37]. Replacing the centripetal acceleration ($\omega^2 R$) with gravitational acceleration (g), we can clearly identify the similarity with the stability analysis for an interface separating a heavier liquid above a lighter underlying phase. As proposed by Plesset and Whipple [38], a simple balance of stresses at the interface can give us a physical scaling for the most unstable wavelength. We imagine that the interface is perturbed by a disturbance with wavelength λ and infinitesimally small amplitude. The respective upward and downward displacement of the lighter and heavier liquid is favored by the direction of the gravity vector and, in the absence of any resisting mechanism, every perturbation with any arbitrary wavelength grows in amplitude and is unstable. However, the presence of interfacial tension between the two immiscible phases leads to a resisting capillary pressure at the interface which tends to keep the interface between the two liquids flat. The driving force for this instability mechanism scales with $\Delta\rho g a$ where a is the amplitude of the wave and the resisting mechanism rises from the capillary pressure P_{cap} that scales with surface tension and the additional contribution to the curvature of the rim $P_{\text{cap}} \sim \sigma a/\lambda^2$. A simple balance between these two suggests that the critical wavelength scales with the capillary length $\lambda_c \sim \sqrt{\sigma/\Delta\rho g}$.

To apply this scaling to our rotary atomization process we need to replace the gravitational acceleration g with the centripetal acceleration $\omega^2 R$. Furthermore, we convert the wavelength λ of the instability to the number of ligaments N observed around the circumference of the cup ($2\pi R$), resulting in the expected scaling

$$N = \frac{2\pi R}{\lambda} \sim \omega\sqrt{\frac{\rho R^3}{\sigma}} \rightarrow N \sim \sqrt{\text{We}}. \tag{6}$$

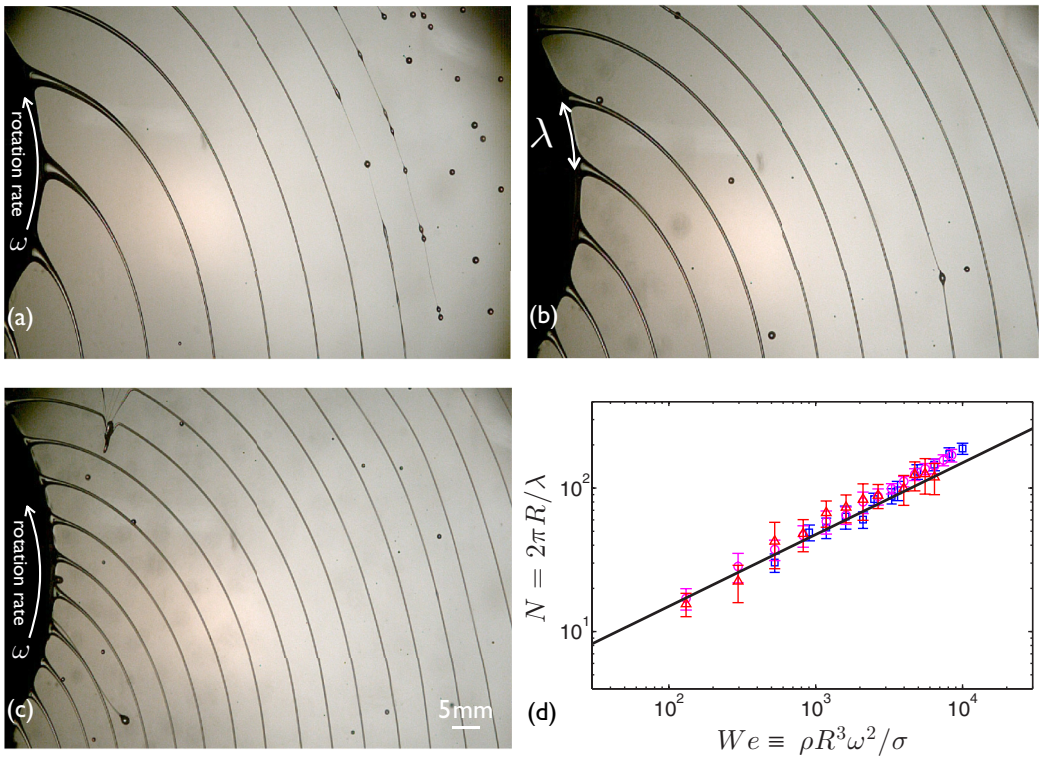

FIG. 5. Silicone oil ($\nu = 100$ cSt) is delivered to the cup at a constant flow rate ($Q = 60$ml/min). Thre snapshots show the number of ligaments formed at three different values of rotation rate [all corresponding to the "ligament" regime in Fig. 3(d)]: (a) $\omega = 62.8$ rad/s, We $\equiv \rho R^3\omega^2/\sigma = 100$, (b) $\omega = 94.2$ rad/s, We $\equiv \rho R^3\omega^2/\sigma = 225$, and (c) $\omega = 157$ rad/s, We $\equiv \rho R^3\omega^2/\sigma = 625$. (d) The number of ligaments N is plotted versus the rotational Weber number We $\equiv \rho R^3\omega^2/\sigma$ for three different silicone oils: (□) {$\nu = 7$ cSt, $\mathrm{Oh}_R = 0.01$}, (○) {$\nu = 100$ cSt, $\mathrm{Oh}_R = 0.17$}, (△) {$\nu = 1000$ cSt, $\mathrm{Oh}_R = 1.67$}. The solid black line shows the predictions of the Rayleigh-Taylor instability analysis $N = \sqrt{\mathrm{We}/3}$.

In fact, Eisenklam [22], inspired by a lecture from G. K. Batchelor, was the first to make this analogy in his study of rotary atomization. He showed that based on the theoretical solution of Taylor [35] for gravitational instability, the scaling relationship described in Eq. (6) has a numerical coefficient of $1/\sqrt{3}$ so that for the most unstable mode:

$$N = \sqrt{\mathrm{We}/3}. \tag{7}$$

Figure 5 shows how the number of ligaments observed in the rotary atomization of silicone oil increases from Fig. 5(a) to 5(c) with increasing rotation rate. This qualitatively agrees with the scaling expected from Eq. (7). We further tested this analysis by measuring the number of ligaments at different rotation rates for three different silicone oils ($\nu = 7$, 100, 1000 cSt). Figure 5(d) shows a summary of the measured data plotted versus different rotational Weber numbers. It is clear that viscosity is not important in controlling the onset of instability and the results for all three different Newtonian fluids agree very well with the prediction of the theoretical model given by Eq. (7) (solid black line).

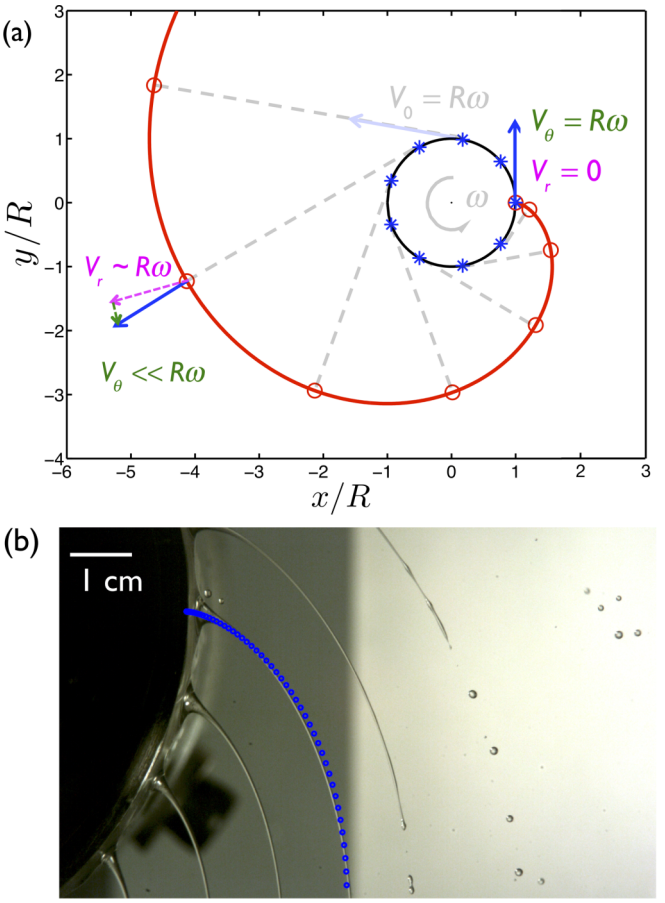

FIG. 6. (a) A simple schematic diagram for the geometry of a single spiral ligament that forms during rotary atomization: The black circle shows the rim of the rotating cup. Individual fluid elements (⋆) leave the rim of the cup, at different times, with a constant speed $V_0 = R\omega$ tangent to the cup, and each follows a straight path-line (indicated by dashed gray lines) that is tangent to the circle at the corresponding point of departure. However, at the current time t_0, the instantaneous locus of all different fluid elements (○) that departed the rim at times $t \leqslant t_0$ forms a continuous spiral pattern (solid red line) that is known as the "*involute of a circle.*" (b) A comparison between the theoretical prediction for the involute of a circle based on Eq. (8) (blue circles) and the experimental profile of a single ligament observed in the rotary atomization of a commercial paint resin. The cup rotation rate is $\omega = 125.6$ rad/s and the fluid, with a zero-shear-rate viscosity of $\eta_0 = 100$ mPa s, is pumped into the cup at a volumetric rate of $Q = 60$ ml/min.

D. Geometry of a single ligament

To understand the kinematics of the flow following the onset of rim instability we need to further investigate the geometry of individual ligaments. As shown in Fig. 6(a), each fluid element leaves the cup with a tangential velocity component $V_\theta = R\omega$. The schematic diagram and the image in Fig. 6 show that close to the cup, the velocity of the fluid elements is dominated by the tangential component V_θ and the radial component V_r is negligible, i.e., initially the velocity of a Lagrangian element is $\mathbf{V_0} \simeq [0, R\omega]$. Assuming a zero radial velocity component at the departure point [39] $V_r(r = R) = 0$, we can see that individual fluid particles leave the rim of the cup, at different times, with a constant speed $V_0 = R\omega$ and they all follow simple straight path-lines that are plotted as dashed gray lines in Fig. 6(a). The component of the velocity projected in the radial direction (using

a global coordinate system centered on the center of the rotating cup) gradually increases as the fluid elements move further from the cup, and eventually this becomes the dominant component of the velocity at large values of r/R. However, at any instant of time t_0, the instantaneous position of all different fluid elements that comprise a single continuous liquid filament which have left the cup at different times in the past $t \leqslant t_0$ form a continuous spiral-like shape (similar to the idea of a rotating "streak-line"). This geometrical shape is known as the "*involute of a circle*" and has been extensively studied in different fields of science. Some of the noteworthy examples include the pioneering works of Christiaan Huygens [40,41] in his study of clocks for addressing the longitude problem in naval navigation and also the design of impulse-less transmission gears by Leonard Euler [42,43]. It can be shown [44] that the spiral shape of the filament that emanates from a certain point x_0, y_0 on the cup at time t_0 has the following parametric equation in Cartesian coordinates:

$$(x - x_0)/R = \cos\phi + \phi \sin\phi - 1, \tag{8a}$$

$$(y - y_0)/R = -\sin\phi + \phi \cos\phi, \tag{8b}$$

where for each fluid element on the spiral, the parameter $\phi = \omega(t_0 - t)$ is the angle that the cup has rotated since the departure of that fluid element from the rim of the cup. Figure 6(b) shows the profile of several ligaments that are formed during the rotary atomization of a viscous paint resin at $\omega = 125.6$ rad/s in a cup of radius $R = 2.5$ cm. The blue circles show the corresponding involute of a circle described by Eq. (8) and this agrees well with the observed spatial profile of an individual ligament. The agreement suggests that even for complex fluids such as paints and resins the kinematics of the initial flow close to the rim can be simply described on the basis of tangential departure of fluid elements from the rotating cup.

E. Kinematics of the flow

To determine the important kinematic measures of the fluid motion in each ligament (e.g., the spatial variations in the velocity profiles and the resulting strain rates) we analyze the trajectory of individual fluid elements within a filament by first assuming that each fluid element leaves the cup with zero radial velocity component and a tangential velocity component equal to the speed of the cup surface as we discussed above. Figure 7(a) shows a pictorial description of the proposed model. We emphasize that these simple kinematics may not be apparent when we look at the spiral-like geometry of a single ligament [Fig. 7(b)] because of the difference between pathlines and streaklines in this unsteady rotating flow. Neglecting the effect of air friction, the velocity of every Lagrangian fluid element along each spiral ligament is a constant vector $\mathbf{V_0}$ with fixed magnitude of $|\mathbf{V_0}| = R\omega$. However, the corresponding radial and tangential components of this velocity expressed in the global coordinate frame $\{r, \theta\}$ centered on the cup vary as the fluid element moves outward away from the spinning cup. A simple geometrical projection provides the following expressions:

$$\frac{V_r}{R\omega} = \frac{\sqrt{r^2 - R^2}}{r}, \tag{9a}$$

$$\frac{V_\theta}{R\omega} = \frac{R}{r}. \tag{9b}$$

So that the speed of any Lagrangian point P along the involute remains $|\mathbf{V_p}| = \sqrt{V_r^2 + V_\theta^2} = R\omega$. Similarly, the angular momentum of each point remains constant and equal to its initial value $\rho\,\mathbf{r} \times \mathbf{V_p} = \rho r V_\theta = \rho R^2 \omega$.

In Fig. 7(b) we show the loci of seven material points along the involute ejected from the rim at fixed times $\Delta t = 2\pi/9\omega$. At time t_0 the material element P initially leaves the rim from position X_0 with purely tangential velocity. The corresponding position of point R_0 on the rim is shown by the corresponding filled triangle (◀). At time t_1 the element P has moved outwards to radius $r_p(t_1)$ and angle $\theta_p(t_1)$ in the global coordinate frame centered on the cup. In this time, however, the point on the rim R_0 (◀) has also rotated through an angle $\theta(R_0) = \omega(t_1 - t_0)$ as shown in Fig. 7(b) and

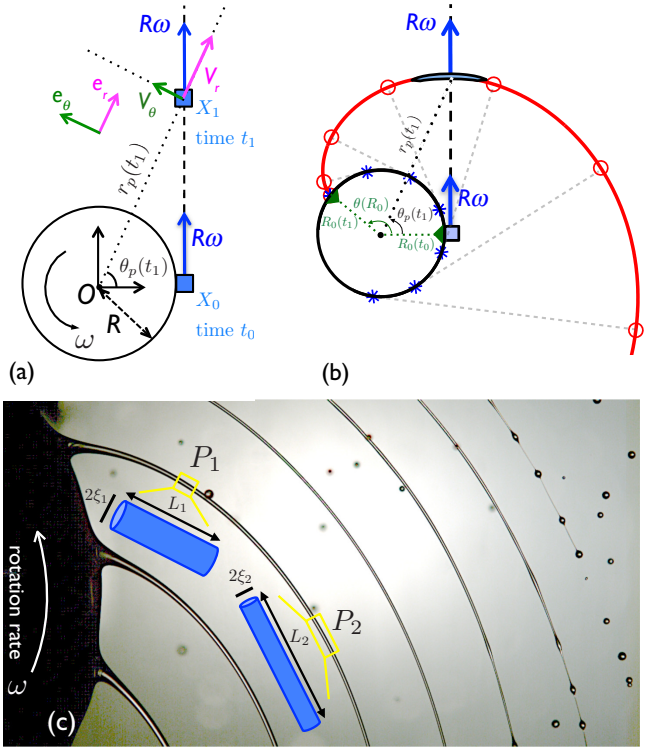

FIG. 7. The kinematics of a single fluid element in (a) pathline and (b) streakline representation separately. In (a), the constant velocity vector of the fluid element (with magnitude $|\mathbf{V_0}| = R\omega$) is projected on the radial and tangential directions and at every moment, based on the radial position r, the corresponding velocity components V_r and V_θ can be calculated using Eq. (9). At time t_0 the material element P initially leaves the rim from position X_0 with purely tangential velocity. At time t_1 the element has moved outwards to radius $r_p(t_1)$ and angle $\theta_p(t_1)$ in the global coordinate frame centered on the cup. In this time, however, the point on the rim R_0 (◀) has also rotated through an angle $\theta(R_0) = \omega(t_1 - t_0)$ as shown in (b) and a sequence of additional material elements have been released at all intermediate times $t_0 < t < t_1$. (c) Illustration and visualization of the continuous elongation of fluid elements as they distance themselves from the cup and move to larger radial positions. The profile of each streakline is the involute of a circle given by Eq. (8) and fluid elements on the involute continue to stretch along the local symmetry axis of the ligament. To conserve the volume of liquid in the element, the axial stretching leads to the gradual thinning of the ligament. Thus, the local thickness $\xi(t)$ of each ligament decreases with increasing distance $r(t)/R$.

a sequence of additional material elements have been released. These fluid elements form a spiral ligament that is shown as an involute of a circle (red line) in Fig. 7(b) and also experimentally visualized in Fig. 7(c). It is clear that material elements are stretched along the symmetry axis of this spiral ligament.

From the velocity field in Eq. (9) we can calculate the strain-rate tensor and find the corresponding eigenvectors. At any given point $\{r, \theta\}$ in the global coordinate frame centered on the cup, it can be shown that the deformation is equivalent to pure elongation along a principal direction $\mathbf{e}_{11} = (R/r)\mathbf{e}_\mathbf{r} - (1 - R^2/r^2)^{1/2}\mathbf{e}_\theta$ where $\mathbf{e}_{11}$ is the unit vector tangent to the symmetry axis of each spiral ligament. Using the parameter ϕ to denote angular distance (or elapsed time) along the spiral [see Eq. (8)], one can also express this principal direction $\mathbf{e}_{11}$ as $\mathbf{e}_{11} = (1 + \phi^2)^{-1/2}\mathbf{e}_\mathbf{r} - \phi(1 + \phi^2)^{-1/2}\mathbf{e}_\theta$. The pure elongation along the symmetry axis of each ligament has a stretch rate

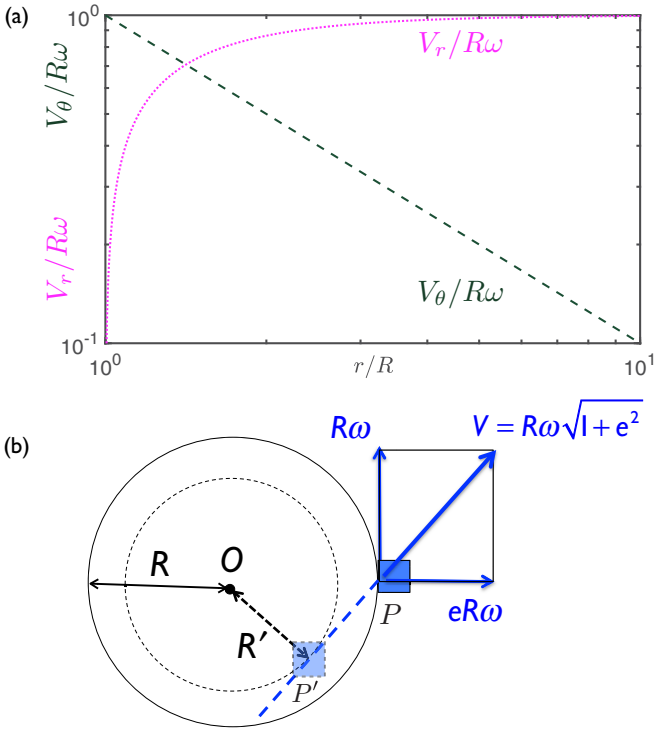

FIG. 8. (a) Plot of the dimensionless radial (pink) and tangential (dark green) components of the Eulerian velocity field for a material element along the involute as a function of r/R. (b) Illustration (not shown to scale) for the idea of the *virtual cup* (dashed circle). Fluid elements with nonzero radial velocity $[V_r(r = R) = eR\omega]$ at the rim of the real cup (a cup with radius R and rotation rate ω), shown by the solid circle, follow a trajectory that is identical to the same element ($P' = P$) leaving a virtual cup with modified radius $R' = R/\sqrt{1+e^2}$ and modified rotation rate $\omega' = \omega(1+e^2)$, shown by the dashed circle.

$\dot{\epsilon}_{11}(r) = \dot{\epsilon}(r)$ that varies spatially in the following way:

$$\dot{\epsilon}(r) = \frac{\partial V_r}{\partial r} + \frac{1}{r}\frac{\partial V_\theta}{\partial \theta} + \frac{V_r}{r} = \frac{\omega}{\sqrt{(r/R)^2 - 1}}, \tag{10}$$

which can also be represented in parametric form as $\dot{\epsilon}(\phi) = \omega/\phi$, where the parameter ϕ increases from zero to higher values along each spiral ligament. In other words, as a fluid element P leaves the cup, due to the kinematics along the spiral ligament, it experiences a continuous shear-free elongational flow aligned along the local axis of the ligament. As indicated schematically in Fig. 7(c), to conserve the volume of each fluid element, the elongation along the ligament, i.e., an increase of length from L_1 to L_2 leads to a related contraction in the thickness (decrease from ξ_1 to ξ_2). As shown by Eq. (10), the rate of elongation decreases with radial distance and eventually becomes negligible at large values of r/R. This qualitatively agrees with the physical picture that the changes in the velocity components and the rate of reduction in the local thickness $\xi(t)$ of the ligaments are much larger in the vicinity of the cup.

At the same time, this functional form of the material stretching shows a singularity at the edge of the cup where $r/R \to 1$. Figure 8(a) shows a plot of the velocity components and their corresponding spatial variation. It is clear that the radial velocity has an infinite rate of change at the edge of the cup, i.e., $\partial V_r/\partial r \to \infty$ as $r/R \to 1$. This singularity is also inherited in the strain rate and Eq. (10) also diverges at $r/R = 1$. This mathematical singularity is not physical and it rises

from the assumption of an identically zero radial velocity at the edge of the cup. The radial velocity at $r/R = 1$, despite being negligible compared to the tangential velocity, is in fact nonzero due to the slow radial outflow of the fluid as it moves axially outwards along the conical cap shown in Fig. 2(a) to form the annular fluid rim of finite thickness.

To establish a more physical model and account for the small nonzero radial velocity of material elements at the cup rim ($r = R$), we consider the situation that would arise if the fluid elements leave the cup with an initial velocity vector that has both a primary tangential component as well as a small, finite radial component. As indicated in Fig. 8(b), the tangential velocity is taken again to be identical to the actual cup speed $R\omega$ and the radial velocity component is a small fraction e of the cup speed $V_r = eR\omega$. As we show in Fig. 8(b), by a simple geometrical transformation we can find the kinematics of the fluid elements along this new involute. Extrapolating (backwards) the velocity vector of this fluid element into the cup we can identify a smaller circle which forms a tangent to this vector. The kinematics of the flow in the new model will be identical to the results of our previous model [Eqs. (9) and (10)] if we replace the original cup [solid black circle in Fig. 8(b)] with the smaller imaginary cup (dashed circle) that has a modified radius $R' = R/\sqrt{1+e^2}$ and a modified rotation rate $\omega' = \omega(1+e^2)$ such that the speed of the fluid element P is unchanged.

Using this simple geometrical idea we can obtain the following equations for the spatial variation of velocity components of a material point at a position $r_p(t) = r$ from the cup:

$$\frac{V_r}{R\omega} = \frac{\sqrt{r^2(1+e^2) - R^2}}{r}, \tag{11a}$$

$$\frac{V_\theta}{R\omega} = \frac{R}{r}, \tag{11b}$$

and the modified expression for the strain rate of a fluid element:

$$\dot{\epsilon}(r) = \frac{\omega(1+e^2)}{\sqrt{(r/R)^2(1+e^2) - 1}}. \tag{12}$$

In Figs. 9(a) and 9(b) we show the evolution in the modified velocity components [Eq. (11)] and the strain-rate field [Eq. (12)], respectively. The singularity in $\partial V_r/\partial r$ as $r/R \to 1$ is now resolved by recognizing that there is a small nonzero radial velocity component. In addition, the stretch rate profile shows a finite maximum strain rate at the edge of the cup $\dot{\epsilon}_{\max} = \omega(1/e + e)$.

It is important to recognize that the parameter e cannot be chosen to have an arbitrary nonzero value but indeed has a physical meaning and can be connected to key physical parameters that are involved in rotary atomization. A simple balance of flow rate for a control volume that contains the entire cup shows that the fluid delivered at a volumetric rate $Q_{\text{in}} = Q$ is balanced by an outflow at the edge of the cup with a corresponding rate of $Q_{\text{out}} = N\pi\xi_0^2 eR\omega$, where N is the number of ligaments of thickness ξ_0. Thus, this simple conservation of mass leads to a physical value for the parameter $e = (Q/R\omega)/(N\pi\xi_0^2)$.

We can also write a differential equation for the spatial evolution of the ligament radius $\xi(r)$. By conserving the volume of a cylindrical element, we can connect the stretch rate along the ligament axis to the radial contraction in the ligament radius $\dot{\xi}(t')/\xi(t') = [-\dot{L}(t')/2L(t')]$ where $t' = (1/\omega')\sqrt{r^2/R'^2 - 1}$ is the the current lifetime of the fluid element which is measured from the virtual moment that the fluid element has left the imaginary cup (with radius R') [45]. This result along with the derived kinematics [Eq. (12)] can be integrated with respect to r and leads to the following expression for radial evolution of the ligament thickness:

$$\frac{\xi(r)}{\xi_0} = \left(\frac{e}{\omega' t'}\right)^{1/2} = \frac{e^{1/2}}{[(r/R')^2 - 1]^{1/4}}. \tag{13}$$

Figure 10 shows the variation in the measured ligament thickness at different radial positions. The measured values are compared with the predictions based on the thinning kinematics of the ligament [Eq. (13)]. The good agreement indicates that each ligament indeed traces the kinematics of a series

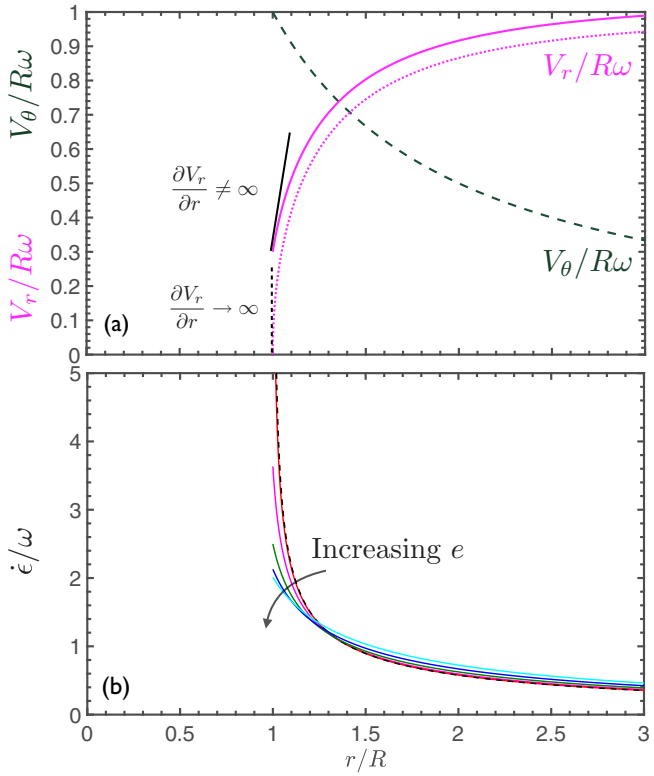

FIG. 9. Theoretical predictions of the kinematics of the flow: (a) Plot of the dimensionless velocity components (shown in pink for V_r and dark green for V_θ) in the case of zero [dashed and dotted lines used, respectively, for V_r and V_θ when $e = V_r(0)/V_\theta(0) = 0$] and nonzero [solid pink line for $e = V_r(0)/V_\theta(0) = 0.3$] initial radial velocity. The profile for the tangential velocity component is independent of e but the radial velocity is modified and with $e > 0$ the singularity in $\partial V_r/\partial r$ at $r/R \to 1$ is removed. (b) Profile of dimensionless stretch rates for different values of e in the range $0 \leqslant e \leqslant 1$. The maximum stretch rate $\dot{\epsilon}_{\max} = \omega(1/e + e)$ occurs at the rim of the cup $r/R = 1$.

of material points described by Eq. (11) and the resulting strain rate along the axis of the ligaments leads to a decrease in the ligament thickness. As the ligaments move outwards from the cup, the local stretching rate and the local thickness both decrease. The radial evolution of these parameters can help us to find the critical position and thickness at which ligaments become unstable due to the action of the capillary forces.

F. Model for predicting the average droplet size

The stability of a cylindrical column, known as the Rayleigh-Plateau instability, has been studied rigorously in the literature [46]. However, as pointed out by several papers on the stability of deforming rims/ligaments [47,48], the dynamics is more complex for a stretching ligament. It is known that a cylindrical fluid ligament can be stabilized by stretching if the imposed elongation rate is faster than the rate of capillary thinning in the ligament [49–51]. Applying this principle to rotary atomization means that capillary perturbations on each spiral ligament only become unstable and begin to grow in amplitude when the local stretch rate $\dot{\epsilon}(r)$ decreases to become comparable to the local rate of capillary thinning $1/\sqrt{8\rho\xi^3(r)/\sigma}$ which is increasing as the ligament thickness $\xi(r)$ decreases. To find the ligament thickness ξ_c at this critical point, we switch to a Lagrangian/temporal

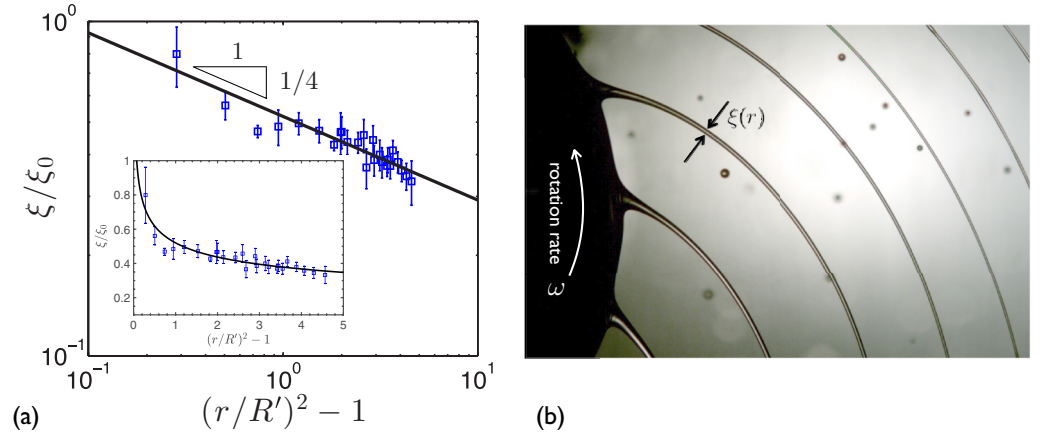

FIG. 10. (a) Measured values of the ligament thickness at different radial positions (blue squares) for a silicone oil (50 cSt) fluid fed into the rotating cup ($\omega = 94$ rad/s) at a volumetric rate of $Q = 1 \times 10^{-6}$ m^3/s corresponding to a rotational Weber number We $= 1712$ and an estimated value of $e = (Q/R\omega)/(N\pi\xi_0^2) \simeq 0.26$ based on measured value of $\xi_0 \simeq 0.37$ mm through image analysis. The solid black line shows the prediction of the analytical model [Eq. (13)] with $e = 0.26$. (b) The thickness profile for individual ligaments are measured from the snapshots that are taken by the high-speed camera. For more quantitative measurements of the ligament thickness, a VZM *zoom imaging* lens (from Edmund Optics) with 60 mm working distance and a 6:1 zoom ratio was used. This results in a final optical resolution of 5 μm/pixel.

description and parametrize both the ligament thickness ξ and the stretch rate $\dot{\epsilon}$ in time t' rather than (unknown) radial position. Equation (13) provides an expression for $\xi(t') = \sqrt{e/\omega' t'}$ which also leads to a temporal parametrization of the local stretch rate $\dot{\epsilon}(t') = -2\dot{\xi}(t')/\xi(t') = 1/t'$. The Lagrangian/temporal description can be easily converted back to the Eulerian/spatial description by replacing t' with $(1/\omega')\sqrt{r^2/R'^2 - 1}$. As the fluid elements move away from the cup (corresponding to higher values of t' and r in the Lagrangian or Eulerian descriptions, respectively) the local stretch rate decreases and the ligaments only become unstable when $\dot{\epsilon}(t'_c) = 1/t'_c \simeq 1/\sqrt{8\rho\xi_c^3/\sigma}$ or in other words when $t'_c \simeq \sqrt{8\rho\xi_c^3/\sigma}$. Inserting this value for t'_c in Eq. (13) gives us the following expression for a critical ligament thickness (at which the ligament becomes unstable to capillary perturbations):

$$\frac{\xi_c}{\xi_0} = \left(\frac{e}{\omega'\sqrt{8\rho\xi_c^3/\sigma}}\right)^{1/2}. \tag{14}$$

Since $e < 1$ we can approximate $e/(1+e^2)$ with e which can itself be replaced with $Q/(N\pi\xi_0^2 R\omega)$. We can also eliminate the number of ligaments $N = \sqrt{\rho R^3\omega^2/3\sigma}$ using Eq. (7) and solve for ξ_c:

$$\frac{\xi_c}{R} = \left[\left(\frac{\sqrt{3}}{\pi\sqrt{8}}\right)\left(\frac{Q/R^2}{R\omega}\right)\left(\frac{\sigma/R}{\rho R^2\omega^2}\right)\right]^{2/7}. \tag{15}$$

This expression describes the critical ligament thickness at which capillary waves start to grow along the thinning ligament. Eggers and Villermaux [46] show that the drops generated from the capillary breakup of an unstable cylinder with a thickness ξ_c have an average radius $\langle d\rangle/2 \simeq 1.88\xi_c$. Thus, the result derived in Eq. (15) can be written in the following form as a prediction for the expected values of average droplet diameter during rotary fragmentation:

$$\langle d\rangle/2R = 1.18\left[\left(\frac{Q/R^2}{R\omega}\right)\left(\frac{\sigma/R}{\rho R^2\omega^2}\right)\right]^{2/7} \sim \mathrm{We}_{\mathrm{convection}}^{1/7}\,\mathrm{We}_{\mathrm{rotation}}^{-3/7}. \tag{16}$$

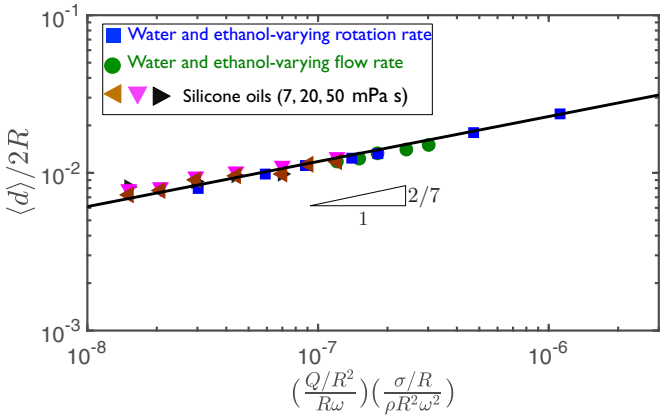

FIG. 11. Measured average droplet diameters for all the Newtonian test liquids normalized by the cup diameter ($\langle d\rangle/2R$) is plotted versus the suggested relevant dimensionless group $\Pi = (\frac{Q/R^2}{R\omega})(\frac{\sigma/R}{\rho R^2\omega^2})$. The solid black line corresponds to the analytical prediction from Eq. (16): $\langle d\rangle/2R = 1.18\{[Q/(R^3\omega)][\sigma/(\rho R^3\omega^2)]\}^{2/7}$.

Figure 11 shows a summary of the measured average droplet diameters for different Newtonian test liquids. Results from experiments performed with three different silicone oils (7,20,50 cSt) and also with the Newtonian ethanol-water mixture are collected at different rotation and flow rates. As the feed rate to the cup is increased the mean diameter increases as $Q^{2/7}$ which is consistent with the empirical exponent of 0.3 obtained from Fig. 4(b). Similarly, as the rotation rate is increased the mean diameter is predicted to decrease as $\omega^{-6/7}$ consistent with the result obtained experimentally in Fig. 4(a). Once plotted in the dimensionless form presented in Fig. 11, it is clear that all the data collapse onto a single functional form depending on the dimensionless group $\Pi = (Q/R^3\omega)(\sigma/\rho R^3\omega^2)$. The prediction of the theoretical model [Eq. (16)] is plotted as a black solid line and shows remarkable agreement with the measured values.

The prediction in Eq. (16) was based on a series of simple physical assumptions and shows good agreement with the experimental measurements. Furthermore, this theoretical model can help rationalize certain power law exponents that have been reported in the literature as empirical correlations [11] and help in developing new applications of rotary atomization. Table III provides a summary for these reported power law exponents. It is clear that the suggested model in this study predicts power law exponents that are all within the range of the reported values in the literature from different empirical correlations. Furthermore, unlike the empirical correlations, the physical origins of this model provides a simple accessible framework that can help researchers in finding novel designs for atomizing geometries or sprayable liquids.

TABLE III. A summary of reported power law exponents (α, β, δ) used in different correlations that are suggested in the literature of rotary atomization for the dependency of average droplet diameter $\langle d\rangle \sim Q^\alpha \omega^\beta D^\delta$ on different parameters.

Reference	Liquid	Feed rate Q	Rotation rate ω	Diameter D
Hege [25]	Various	–	−1.0	−0.5
Oyama *et al.*[26]	Water	0.2	−1.0	−0.30
Kamiya and Kayano[21]	Water	0.33	−1.0	−0.5
Ryley[27]	Water	0.19	−1.41	−0.66
Dombrowski and LLoyd[11]	Oil	0.33	−1.32	−1.22
Present work	Various	$2/7 \simeq 0.29$	$-6/7 \simeq -0.86$	$-5/7 \simeq -0.71$

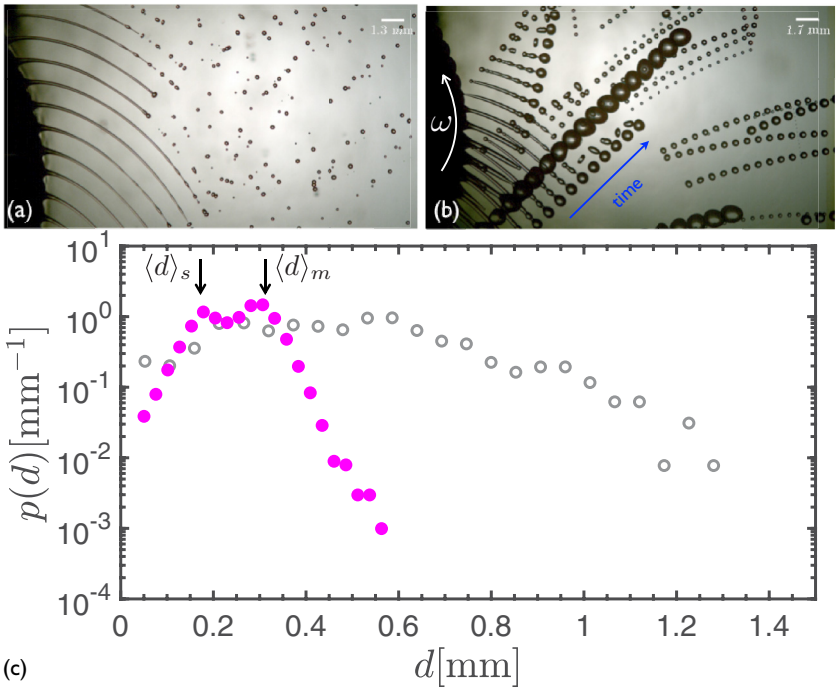

FIG. 12. Rotary atomization for the Newtonian solvent (ethanol-water 90%–10% wt. mixture, $\eta =$ 1 mPa s, $\mathrm{Oh}_R \equiv \eta/\sqrt{\rho R \sigma} = 1.45 \times 10^{-3}$) with the cup spinning at two different values of rotation rate: (a) Ligament formation state at $\omega = 219.8$ rad/s, $\mathrm{We} \equiv \rho R^3 \omega^2/\sigma = 6442.8$ corresponding to $\Pi_1 = 227$ and $\Pi_2 = 0.0015$ in Fig. 3(d). The image shows an overlay of two consecutive frames each $\Delta t = 0.4$ ms apart from each other. (b) Drop formation state at $\omega = 78.5$ rad/s, $\mathrm{We} \equiv \rho R^3 \omega^2/\sigma = 821.8$ corresponding to $\Pi_1 = 81$ and $\Pi_2 = 0.0015$ in Fig. 3(d). The image shows an overlay of sixteen consecutive frames each $\Delta t = 1$ ms apart from each other to illustrate the droplet rupture and coalescence processes. (c) Corresponding droplet size distributions $p(d)$ are plotted as filled circles (•) for the ligament formation state [shown in (a)] and as open gray circles (○) for the drop formation state (shown in (b)). In each case over 10 000 droplets were analyzed to calculate the size distribution.

It is worth noting that after obtaining the expression in Eq. (16), we discovered a similar prediction has already been reported in a completely separate and independent work from the Russian fluid mechanics community. Dunskii and Nikitin [52] derive a final analytical expression in their work that is similar to Eq. (16). However, this work has remained undiscovered and up to the time of writing there appear to be no citations of this work to the best of our knowledge. We thus note that despite the fact that we independently derived the model and checked it with our own experimental measurements, we can not claim to be the first to derive this analytical prediction.

In addition to understanding how the average droplet diameter changes, the resulting size distributions resulting from the fragmentation process is of great importance in many different industries. In the following section we focus on different aspects of the size distribution of droplets expected for Newtonian fluids.

VI. DROPLET SIZE DISTRIBUTIONS-NEWTONIAN LIQUIDS

To study the fragment size distributions in the rotary atomization, we analyzed the recorded high-speed movies and collected a large population of droplets (typically $\sim O(10^4)$ droplets for each experiment). In Fig. 12 we show the probability density $p(d)$ (i.e., the likelihood of finding

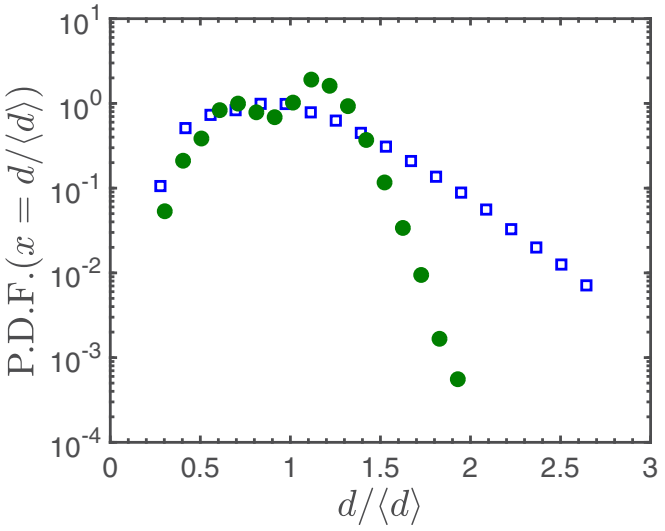

FIG. 13. Normalized droplet size distributions for the Newtonian solvent used in rotary atomization (green filled circles ●) and the corresponding distribution obtained the air-assisted atomization (blue open square □). The liquid atomized in the rotary test is the ethanol-water (90%–10% wt.) mixture ($\mathrm{Oh}_R = 1.45 \times 10^{-3}$, $\mathrm{We} = 1.32 \times 10^4$). The tested liquid in the air-assisted atomization process is a water-glycerol (60%–40% wt.) mixture ($\mathrm{Oh}_R = 4 \times 10^{-3}$, $\mathrm{We} = \rho_{\mathrm{air}} V_{\mathrm{air}}^2 R/\sigma = 277$).

droplets at size d) of the measured size distributions for the Newtonian ethanol-water mixture at two different rotational rates corresponding to $\Pi_1 = 81$ and $\Pi_1 = 227$ in Fig. 3(d). At the higher rotation rate ligaments are formed and the disintegration into droplets happens in the ligament formation regime [Fig. 12(a)]. Meanwhile, as is clear from the sequence of 16 overlaid frames in Fig. 12(b), for the lower rotation rate, the fragmentation process happened in the drop formation regime. Corresponding size distributions for the ligament and the drop formation regimes are plotted in Fig. 12(c) in filled magenta and hollow gray symbols, respectively. It is clear that the atomization ligament formation regime leads to a markedly narrower size distribution. This confirms the general idea that, due to the more organized and highly structured shape of the spiral ligaments, it is preferable to operate a rotary atomizer in this regime. A more precise examination of the magenta data points in Fig. 12(c) also verify the existence of two peaks in the measured size distributions.

The emergence of a double peak in the droplet size distributions is not observed in measurements of size distributions in air-assisted atomization (see Refs. [33,53,54]). However, a direct comparison of the measured size distributions between air-assisted atomization (data from Ref. [33]) and rotary fragmentation can give us a better sense about the benefits of rotary atomization. In Fig. 13 we plot the normalized probability distribution function (PDF) as a function of the scaled droplet size $x = d/\langle d \rangle$. It is clear that despite showing the double peak in the size histograms, the rotary fragmentation process generates overall a much narrower size distribution. A larger fraction of the total droplets are distributed close to the average diameter and a much lower fraction are significantly larger than the average size. In fact, it is 100 times more probable to find a droplet of twice the average size (i.e., $x = 2$) in the air-assisted fragmentation process compared to rotary atomization. A known measure for the breadth of the droplet size distributions is the ratio $D_{32}/\langle d \rangle$, where D_{32} is the Sauter mean diameter $D_{32} = \sum d_i^3 / \sum d_i^2$ which can be calculated from the measured droplet sizes d_i. Monodisperse size distribution have values of $D_{32}/\langle d \rangle$ very close to unity and polydispersity increases this ratio. For the droplet population data in Fig. 13, we obtain values of $D_{32}/\langle d \rangle = 1.33$ and $D_{32}/\langle d \rangle = 1.13$ for the air-assisted and rotary atomization process, respectively.

This encouraging result suggests that in rotary atomization there is a higher level of control of the droplet size distribution through the spiral geometry of the ligament patterns. It also indicates

that the initial corrugations on the ligaments are much smaller in amplitude [55]. Indeed, visual examination of the high speed images in Figs. 7(c) and 12(a) show the ligaments are relatively unperturbed and smooth until the local straining rate drops below the critical value beyond a certain radius, and even after that a set of smooth and periodic capillary waves appear on each ligament leading ultimately to pinch off and drop formation. This is very different from the violent nature of air-assisted atomization in which the random fluctuations of the surrounding high-speed air flow generates higher levels of initial corrugation on the ligaments and this ultimately sets the final droplet size distributions [33,55].

The benefits of rotary atomization highlight the need for a better physical understanding of the associated fragmentation process. The appearance of a bimodal size-distribution in rotary atomization has been reported in literature [21,26,56–58] but a physical understanding of this effect remains incomplete.

To understand the origin of the bimodal distribution, we study the final ligament breakup stage in more detail. As indicated in Figs. 12(a) and 12(c), the two individual peaks are related to the coexistence of both a primary distribution (with average diameter $\langle d \rangle_m$) and a satellite droplet distribution (with average diameter $\langle d \rangle_s$). The primary droplets are the result of the growth of capillary waves on the ligaments. These capillary waves grow in amplitude and two neighboring peaks lead ultimately to the formation of two primary droplets. However, the elongated connecting filament between the two main drops does not entirely empty its volume into these primary droplets and at the pinch-off point it forms an elongated and corrugated filament that goes through a secondary fragmentation process. Satellite droplets are the consequence of this secondary fragmentation process which happens at smaller length scales than the primary atomization events.

In Figs. 14(a), 14(b) and 14(c) we show a sequence of images illustrating satellite formation in the case of a more viscous silicone oil ($\nu = 50$ cSt). We can clearly see that while the primary fragmentation process leads to the appearance of the main droplets, the breakup of the connecting filaments between each pair of main droplets controls the secondary fragmentation on a smaller length scale. This two scale process can be analyzed quantitatively by studying the measured size distributions and then comparing them to the behavior of Γ distributions. Villermaux and coworkers [55] have argued that Γ distributions are the asymptotic distributions expected in a coalescence-based fragmentation scenario and this has been validated with experiments in numerous studies of liquid fragmentation [33,49,50,53,59–64]. In fact, in several works [50,62], Villermaux and coworkers observe similar cases in which both a primary and a secondary fragmentation process happen simultaneously giving rise to bi-modality in the final size distributions. Villermaux and Bossa [62] suggest that a linear superposition of two separate Γ distributions is sufficient to capture the phenomenon in detail:

$$p(d) = \frac{a_m}{\langle d \rangle_m} \Gamma(n_m, x = d/\langle d \rangle_m) + \frac{a_s}{\langle d \rangle_s} \Gamma(n_s, x = d/\langle d \rangle_s). \tag{17}$$

The first term describes the breadth of the distribution of main droplets in the primary fragmentation process and the second term describes the secondary fragmentation process, which happens at smaller scales.

Figure 14(d) shows a fit of the proposed model [Eq. (17)] to the measured size distributions. The close agreement shows that the rotary atomization process can indeed be well described as the superposition of a main and a secondary disintegration event which happen at two different scales.

To further investigate this, we recorded all the droplet sizes for four different Newtonian test liquids, each of them being atomized at different rotation rates. In Fig. 15 we show a summary of the data for the ethanol-water mixture and three different silicone oils (7,20,50 cSt). For each liquid the measured sizes at different rotation rates are all normalized by the size of the main droplet diameter ($\langle d \rangle_m$) obtained at that rotation rate. The self-similarity between the superposed distributions suggests that increasing the rotation rate decreases both the main and the satellite droplet size almost equally. In other words, the nature of the two separate fragmentation processes does not change with rotation rate, as long as rotary atomization happens in the ligament formation

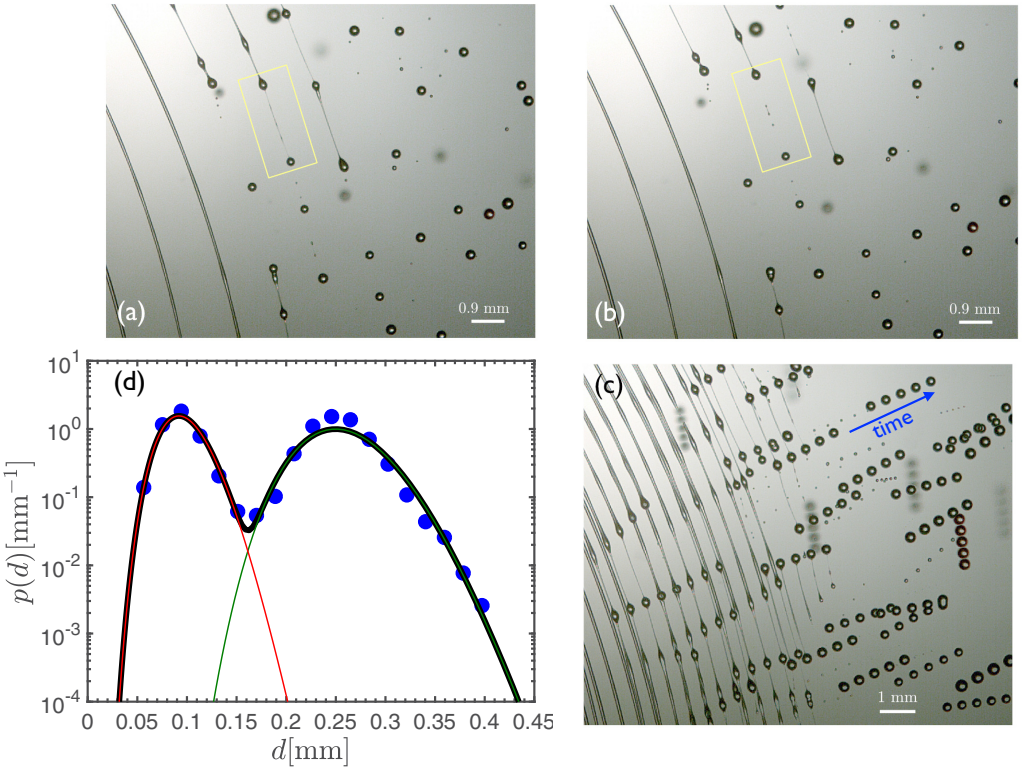

FIG. 14. Formation of small satellite droplets in the final stage of ligament breakup. The tested liquid is a viscous silicone oil ($\nu = 50$ cSt, $\mathrm{Oh}_R = 7.3 \times 10^{-2}$) and it is delivered with a rate of $Q = 60$ ml/min into the cup that is rotating at $\omega = 125.6$ rad/s, $\mathrm{We} = 2104$. (a, b) Two consecutive snapshots of the fragmentation with $\Delta t = 0.2$ ms between them. The viscous connecting filament in the yellow box is clearly stretched before final pinch-off [see (a)] and after the pinch-off event [see (b)] the volume of the fluid in the filament retracts and forms one or two satellite droplets. (c) An overlay of five consecutive frames, with $\Delta t = 0.2$ ms. It is clear to see that while the fragmentation process leads to a relatively mono-disperse group of *main* droplets, there also exists a considerable group of smaller *satellite* droplets. (d) Measured droplet size distributions for this case (blue filled circles •) shows the appearance of two separate peaks which correspond to the size of the main and the satellite droplets in the fragmentation event. The black solid line is the sum of two separate Γ distributions [Eq. (17)] with $a_s = 0.39$, $\langle d \rangle_s = 0.09$ mm, $n_s \simeq 17$ (the red line) and $a_m = 0.61$, $\langle d \rangle_m = 0.24$ mm, $n_m \simeq 33$ (the green line).

regime of Fig. 3(d). Furthermore, we can clearly see that fits to the theoretical model [Eq. (17)] can capture the details of the size distributions for all the tested liquids at different rotation rate. We can also see that, as we increase the viscosity of the test liquid, the location of the secondary peak relative to the primary droplet peak shifts to smaller values (i.e., $\langle d \rangle_s / \langle d \rangle_m$ decreases) but the relative number of small satellite droplets distributed around $\langle d \rangle_s$ increases with increasing viscosity. This suggests that for more viscous liquids, longer and thinner filaments form between the main droplets leading to smaller and more numerous satellite droplets. We will quantify this by a simple model in the following sections.

VII. ROTARY ATOMIZATION OF VISCOELASTIC LIQUIDS

Recognizing that dilute polymer solutions can further stabilize long and thin filaments through the presence of large elastic stresses in extensionally dominated flows, we also investigated the

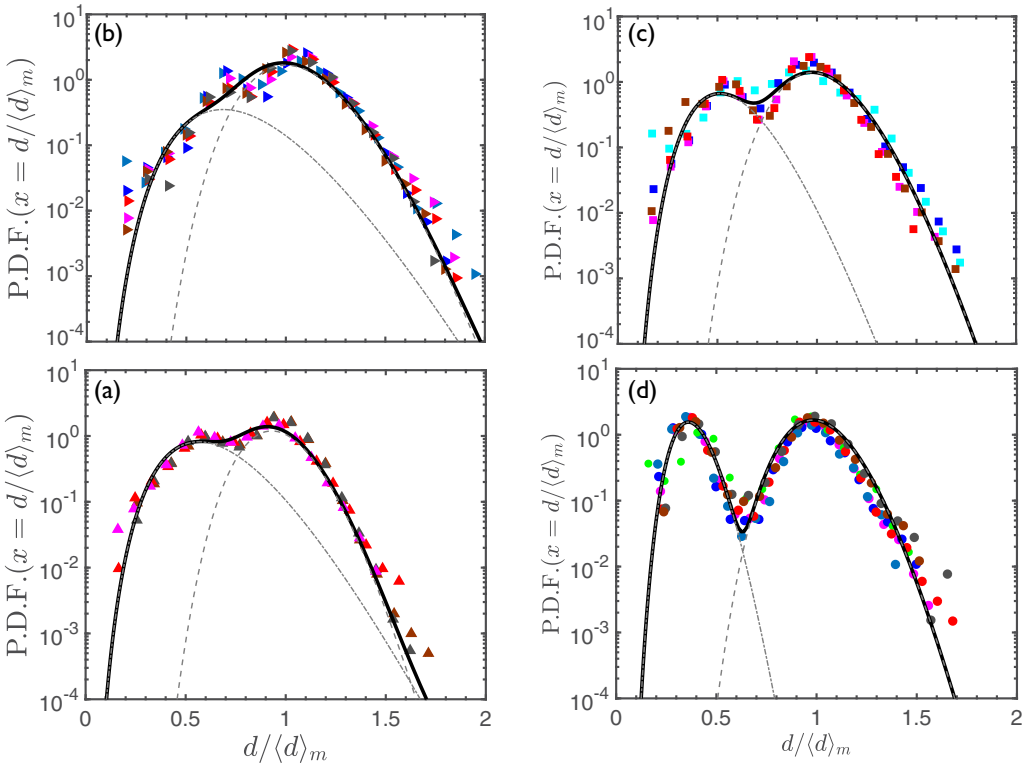

FIG. 15. Droplet size distributions for the rotary atomization of Newtonian test liquids: (a) Ethanol-water (90%–10%wt., $\mathrm{Oh}_R = 1.45 \times 10^{-3}$) mixture; measured size distributions at four different rotation rates {We = 6443}(▲), {We = 8415}(▲), {We = 10650}(▲), and {We = 13149}(▲). (b) Silicone oil ($\nu = 7$ cSt, $\mathrm{Oh}_R = 1.02 \times 10^{-2}$); measured size distributions at six different rotation rates {We = 3287}(▶), {We = 4736}(▶), {We = 6443}(▶), {We = 8415}(▶), {We = 10650}(▶), and {We = 13150}(▶). (c) Silicone oil ($\nu = 20$ cSt, $\mathrm{Oh}_R = 2.90 \times 10^{-2}$); measured size distributions at five different rotation rates {We = 2104}(■), {We = 4736}(■), {We = 6443}(■), {We = 8415}(■), and {We = 10650}(■). (d) Silicone oil ($\nu = 50$ cSt, $\mathrm{Oh}_R = 7.25 \times 10^{-2}$); measured size distributions at seven different rotation rates {We = 1183}(●), {We = 3287}(●), {We = 4736}(●), {We = 6443}(●), {We = 8415}(●), {We = 10650}(●), and {We = 13150}(●). For each Newtonian liquid, we can see that normalizing the measured droplet sizes with the measured average size of the main droplet $\langle d\rangle_m$ at a given Weber number shifts all of the distributions for a given fluid to a single curve. Each distribution is a superposition of a Γ distribution around the satellite droplet size $\langle d\rangle_s(-.-)$ and another around the main droplet size $\langle d\rangle_m(--)$. Fitting Eq. (17) to the data (black solid lines), the following fit parameters are extracted: $\{\langle d\rangle_s/\langle d\rangle_m, a_s, n_s, a_m, n_m\}$= (a) {0.76, 0.13, 12, 0.87, 18}, (b) {0.72, 0.06, 7, 0.94, 29}, (c) {0.58, 0.30, 15, 0.70, 60}, and (d) {0.38, 0.39, 17, 0.61, 33}.

behavior of a series of weakly viscoelastic test fluids. As discussed earlier, many industrial materials such as paints also exhibit non-Newtonian elongational properties, and in this section we study the performance of this class of complex fluids during the process of rotary atomization.

As shown by Keshavarz *et al.* [31], the addition of small concentrations of flexible high molecular weight polymer does not affect the shear viscosity in the dilute regime compared to the drastic increase in elongational viscosities. Thus, these dilute polymeric solutions show Newtonian-like behavior in shear, but resist strong elongational deformations. Figure 16 shows that the addition of 0.01wt.% of PEO with a mass average molecular weight of $M_w = 1 \times 10^6$ g/mol (corresponding to $c/c^* = 0.07$) to the solvent (90%–10% ethanol-water mixture) can significantly change the

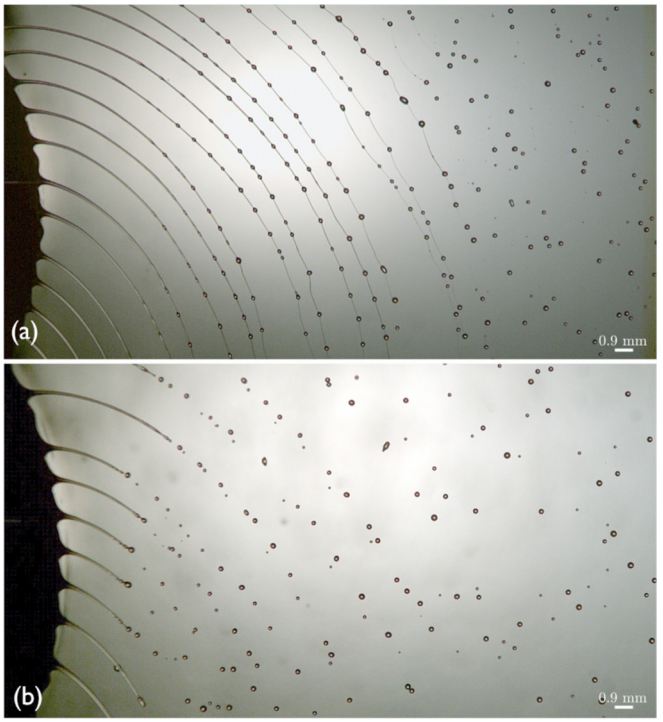

FIG. 16. Visualization of the fragmentation process with the cup rotating at $\omega = 251.2\,\text{rad/s}$ and the test liquids delivered at a rate of $Q = 60\,\text{ml/min}$. Images show the rotary atomization for (a) the viscoelastic fluid (PEO with $c = 0.01\%$ wt., $M_w = 10^6$ g/mol in the ethanol-water solvent) and (b) The ethanol-water solvent (90%–10% wt.) with $\eta_s = 0.001\text{Pa}\,\text{s}$. After the drops are formed on the ligaments, the connecting filaments between the drops of Newtonian solvent break up very fast. However, due to the enhanced elongational viscosity of the dilute polymer solution, the viscoelastic filaments stretch contiguously and resist the pinch-off process which leads to the formation of thinner stringy filaments.

dynamics of fragmentation. While the ligament spacing and the main droplet diameter is almost the same size as observed for the corresponding Newtonian solvent shown in Fig. 16(b), the appearance of elongated filaments in the viscoelastic case is in marked contrast with the atomization performance of the ethanol-water solvent mixture. To quantify our results, we measured both the average droplet diameters for all three viscoelastic test liquids (tabulated in Table II) and the corresponding droplet size distributions.

A. Average droplet size

Figure 17 shows a summary of the average droplet diameters for the three PEO solutions and the corresponding Newtonian solvent. It is clear that the average diameters for all viscoelastic solutions remain very close to the corresponding values for the Newtonian solvent. In fact, the data collapse on the same dimensionless master curve and agree well with the prediction of our previously proposed model [Eq. (16)].

This suggests that the critical thickness of the primary spiral ligaments at onset of the breakup process (ξ_c) is unaffected by the viscoelastic properties of the fluid. The value of ξ_c is set primarily by the linear stability analysis of the liquid rim at the edge of the rotary cup under the action of capillary forces. In this region the fluid elements have not yet been strongly stretched and the rheology is essentially unchanged from that of the solvent. At the same time, it is known that the

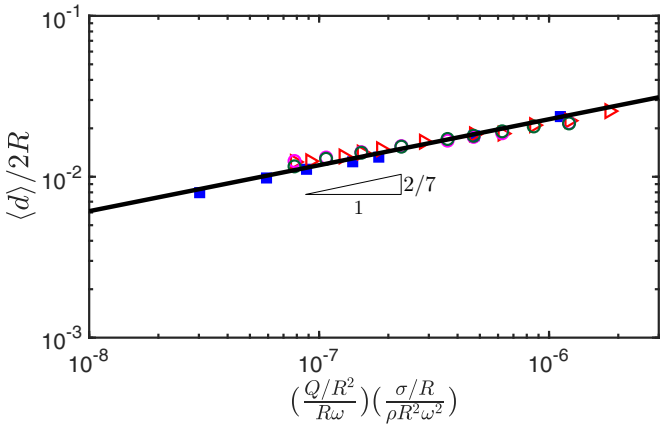

FIG. 17. Evolution in the average diameters measured for the Newtonian solvent (■) and all of the viscoelastic test liquids: PEO $c = 0.01\%$ wt. $M_w = 300$ kg/mol (○), PEO $c = 0.05\%$ wt. $M_w = 300$ kg/mol (○) and PEO $c = 0.01\%$ wt. $M_w = 10^3$ kg/mol (▷). Results are normalized by the cup diameter $\langle d\rangle/2R$ and plotted versus the suggested relevant dimensionless group $\Pi = (\frac{Q/R^2}{R\omega})(\frac{\sigma/R}{\rho R^2\omega^2})$. The solid black line corresponds to the analytical prediction from Eq. (16).

values of the critical growth rate and wavelength in the linear stability analysis of a viscoelastic thread are weakly affected by elongational properties [31,65]. This explains the fact that for these very dilute solutions the average measured droplet diameters are almost unchanged with the addition of viscoelasticity. Thus, similar to Newtonian solvents, the average droplet diameter for weakly viscoelastic fluids follows the same dimensionless scaling that has been described in Eq. (16); i.e., $\langle d\rangle/R \sim \mathrm{We}_{\mathrm{convection}}^{1/7}\mathrm{We}_{\mathrm{rotation}}^{-3/7}$.

B. Droplet size distributions-viscoelastic liquids

In addition to the average droplet size, the droplet size distributions for each viscoelastic test liquid were measured at different rotation rates.

In Fig. 18 we show the droplet size distributions for the 0.01% wt. $M_w = 10^6$g/mol PEO solution (at $c/c^* = 0.07$). As discussed in the previous section, the average droplet diameters are almost unchanged by addition of viscoelasticity but the corresponding size distributions show clear differences for smaller droplet sizes close to the mean satellite droplet diameter $d \sim \langle d\rangle_s$. The overall average diameter $\langle d\rangle$ does not change much from modifications of the droplet size distributions at smaller scales since smaller droplet diameters contribute much less to the overall average than the larger values ($\langle d\rangle_s/\langle d\rangle_m \sim 0.3 < 1$). Nevertheless, compared to the Newtonian solvent, the dilute polymer solution shows a more pronounced peak at lower sizes that has been shifted to smaller values of $\langle d\rangle_s/\langle d\rangle_m$. It is interesting to note that despite this clear difference, the behavior of the two size distributions is almost identical at larger sizes $d \geqslant \langle d\rangle_m$. This again shows that the main droplet distribution and the corresponding fragmentation dynamics is set by the linear stability of the initial spiral ligaments which are substantially unaffected by the nonlinear effects of viscoelasticity. However, the enhanced nonlinear elongational stresses in the polymer solutions change the thinning dynamics of the secondary filaments that are formed between the main droplets and delay their corresponding breakup time. This retardation in the breakup time results in longer thinner filaments and is reflected in the secondary fragmentation process by changes in the size and the number of the satellite droplets formed. A superposition of two separate Γ distributions [Eq. (17)] can again be fitted to the data and the resulting fit is shown by the solid red line which indicates a much lower value of $\langle d\rangle_s$ and also a much broader secondary droplet size distribution (corresponding to lower values of n_s).

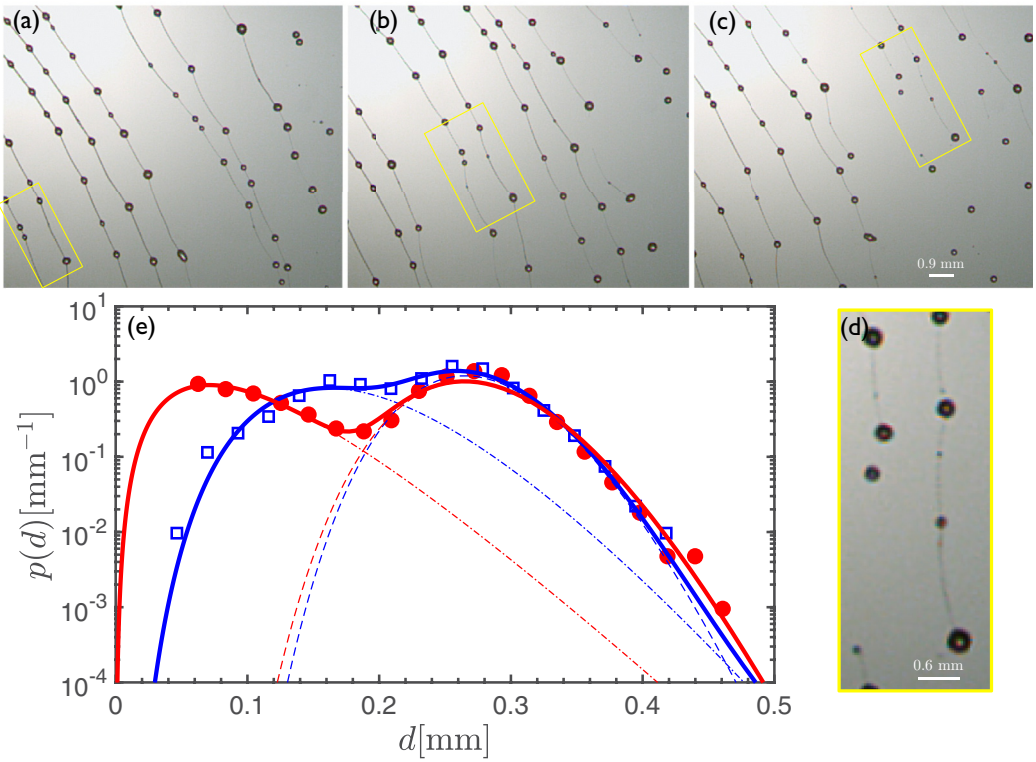

FIG. 18. Breakup dynamics of viscoelastic filaments formed during the rotary atomization process for a PEO solution with $M_w = 10^6$ g/mol and $c = 0.01\%$ wt. ($\mathrm{Oh}_R = 1.45 \times 10^{-3}$, $\mathrm{De}_R = 5.0 \times 10^{-3}$). Images (a), (b), and (c) are taken with $\Delta t = 1$ ms spacing in time. As shown by the yellow box, two neighboring droplets on adjacent ligaments are connected to each other by an elongated fluid filament of highly extensible fluid that resists pinch off and finally transforms to a very thin cylindrical thread. (d) After this thin elastic filament finally pinches off from the connecting drops, it forms a number of very small satellite droplets. (e) The corresponding size distribution are shown by red filled circles (●) and are compared to the corresponding size distributions for the Newtonian solvent (□). The solid lines are the fits of Γ distributions. Each fit is a superposition of two independent Γ distributions [Eq. (17)], one for the smaller droplets that are scattered around the average satellite droplet diameter $\langle d \rangle_s$ (---) and another for the larger droplet sizes distributed around the primary drop diameter $\langle d \rangle_m$ (- -). Parameters extracted from the fits have the following values: for the Newtonian solvents, $a_s = 0.13$, $\langle d \rangle_s = 0.21$ mm, $n_s \simeq 12$, $a_m = 0.87$, $\langle d \rangle_m = 0.27$ mm, $n_m \simeq 18$ and for the viscoelastic solution $a_s = 0.49$, $\langle d \rangle_s = 0.09$ mm, $n_s \simeq 4$, $a_m = 0.51$, $\langle d \rangle_m = 0.27$ mm, $n_m \simeq 40$.

In Figs. 19(a), 19(b) and 19(c) we show the corresponding distributions for the three different PEO solutions at increasing values of the intrinsic Deborah number De_R [see Eq. (4)]. In each figure we present results for a range of different Weber numbers and scale the abscissa by the measured mean diameter $\langle d \rangle_m$ which varies with We according to Eq. (16). For each liquid, the droplet distributions measured at different rotation rates again superpose, demonstrating that increasing the rotation rate of the cup shifts both distributions to smaller values. Comparing Figs. 19(a), 19(b) and 19(c) it is also clear that with increasing viscoelasticity the secondary peak in the size distributions shifts to smaller values of $\langle d \rangle_s / \langle d \rangle_m$. For clarity, only Fig. 19(d) provides a visual comparison between the measured size distributions for viscoelastic fluids and the corresponding best fit for the Newtonian solvent (dash-dotted line). For the least elastic PEO solution ($c = 0.01\%$ wt., $M_w = 300 \times 10^3$ g/mol corresponding to $\tau_E = 68$ μs and $\mathrm{De}_R = 4 \times 10^{-4}$) the droplet size distribution is almost identical to the corresponding PDF for the Newtonian solvent. The more elastic PEO

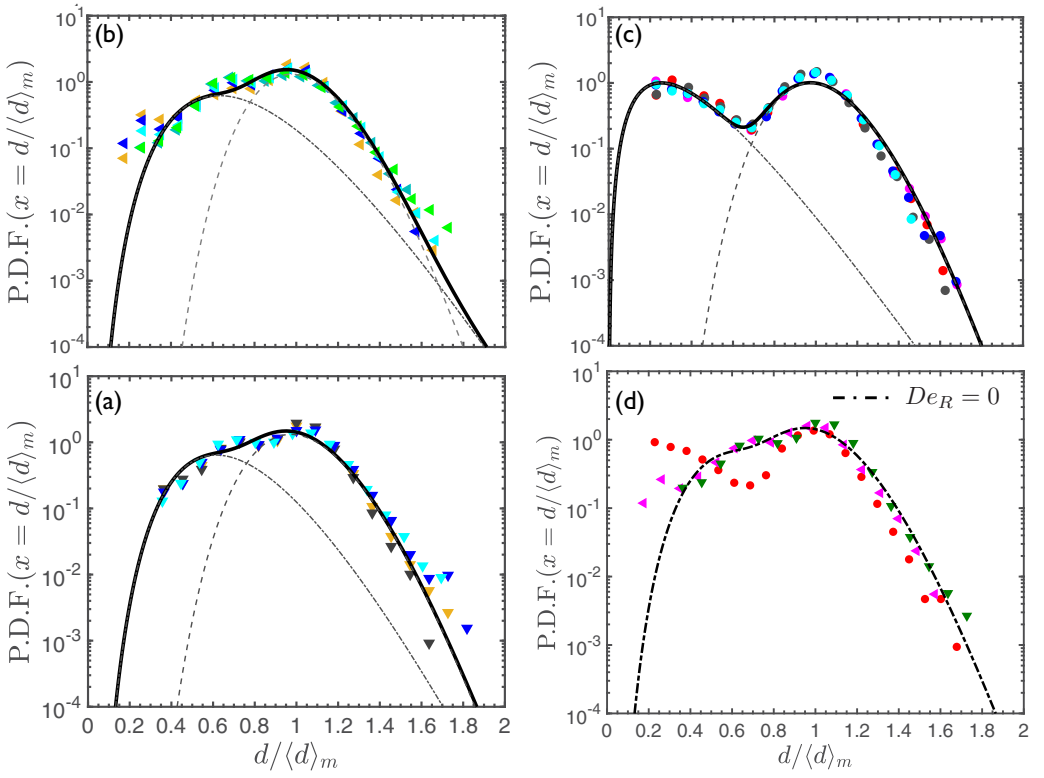

FIG. 19. Droplet size distributions plotted for the rotary atomization of viscoelastic liquids: (a) PEO 0.01% wt. $M_w = 300 \times 10^3$ g/mol solution ($\mathrm{Oh}_R = 1.45 \times 10^{-3}$, $\mathrm{De}_R = 0.4 \times 10^{-3}$); measured size distributions at four different rotation rates {We = 6443}(▼), {We = 8415}(▼), {We = 10650}(▼), and {We = 13150}(▼). (b) PEO 0.05% wt. $M_w = 300 \times 10^3$ g/mol solution ($\mathrm{Oh}_R = 1.45 \times 10^{-3}$, $\mathrm{De}_R = 0.6 \times 10^{-3}$); measured size distributions at five different rotation rates {We = 3977}(◀), {We = 4736}(◀), {We = 6443}(◀), {We = 8415}(◀), and {We = 10650}(◀). (c) PEO 0.01% wt. $M_w = 10^6$ g/mol solution ($\mathrm{Oh}_R = 1.45 \times 10^{-3}$, $\mathrm{De}_R = 5.0 \times 10^{-3}$); measured size distributions at five different rotation rates {We = 7396}(●), {We = 8415}(●), {We = 9500}(●), {We = 11870}(●), and {We = 13150}(●). Black solid lines are the corresponding fits, each of which is a summation of two Γ distributions. Each fit is a linear superposition of a Γ distribution around the satellite droplet size $\langle d\rangle_s$ (−·-) and another Γ distribution around the main droplet size $\langle d\rangle_m$(−−). Fitting Eq. (17) to the data, the following fit parameters are extracted: $\{\langle d\rangle_s/\langle d\rangle_m, a_s, n_s, a_m, n_m\}$= (a) {0.70, 0.13, 12, 0.87, 18}, (b) {0.67, 0.39, 11, 0.61, 42}, and (c) {0.34, 0.49, 4, 0.51, 40}. (d) A comparison between the size distributions of different viscoelastic liquids atomized at a fixed rotation rate {We = 8415}: PEO 0.01% wt. $M_w = 300 \times 10^3$ g/mol (▼), PEO 0.05% wt. $M_w = 300 \times 10^3$ (◀), and PEO 0.01% wt. $M_w = 10^6$ g/mol (●). The broken black line is the fit for the size distributions of the Newtonian solvent at same Weber number [Fig. 14(a)].

solutions ($c = 0.05\%$wt. $M_w = 300 \times 10^3$ g/mol and $c = 0.01\%$ wt., $M_w = 10^6$ g/mol) show a measurably different behavior which is more pronounced around smaller droplet sizes close to $\langle d\rangle_s$. Fits of the Γ distributions to the data for the most elastic PEO solution ($\mathrm{De}_R = 5.0 \times 10^{-3}$) also suggest that in the secondary fragmentation $n_s \to 4$. This suggests that the filaments connecting the main droplets approach the limiting bound of maximum corrugation, consistent with earlier reported results for ligament-mediated fragmentation in the process of air-assisted atomization [33]. The magnified view of the stretched filament in Fig. 18(d) shows the appearance of relatively

large primary beads that are connected to each other by very thin strings. This beads-on-a-string structure increases the level of the geometrical corrugations and results in progressively broader size distributions around $\langle d \rangle_s$ [33].

VIII. TOY MODEL FOR PREDICTING THE SIZE OF SATELLITE DROPLETS

To help understand the dynamics of the secondary fragmentation process, we introduce a simplified toy model that enables us to predict the size ratio $\langle d \rangle_s / \langle d \rangle_m$between the satellite and the main droplet and how it varies with fluid viscoelasticity. We assume that when capillary waves start to appear on the main spiral ligament the fluid filament that connects the two neighboring wave crests is cylindrical with thickness $2h_0$ and length L_0. As the waves grow, the two peaks develop to form the main droplets shown in Fig. 18(d) and the connecting filament keeps stretching until one, or both, of the thin necks that connect to the primary droplets pinches off. Assuming that the volume of the filament is constant during this process, we can write the following:

$$l(t)h(t)^2 = l_0 h_0^2 \rightarrow \frac{h_0}{h(t)} = \sqrt{\frac{l(t)}{l_0}} = \sqrt{1 + \dot{\epsilon}_c t}, \tag{18}$$

where $\dot{\epsilon}_c = 1/\sqrt{8\rho\xi_c^3/\sigma}$ is the critical capillary stretch rate at which the capillary waves start to emerge and grow (see Sec. VII). Since the size of the primary droplets is set when the capillary instabilities initiate on the spiral ligament we can assume that $\langle d \rangle_m \sim h_0$. Similarly, the satellite droplet diameter is set by the secondary fragmentation process on a smaller scale and thus $\langle d \rangle_s \sim h(t_{\text{pinch-off}})$, where $t_{\text{pinch-off}}$ is the time at which the connecting necks between the filament and the main drops pinch off. Thus,

$$\frac{\langle d \rangle_m}{\langle d \rangle_s} = \frac{h_0}{h(t_{\text{pinch-off}})} \tag{19}$$

Based on existing scalings published in the literature [46], we know that the pinch-off time can be delayed by either enhanced viscous or elastic stresses. For viscous Newtonian solutions $t_{\text{pinch-off}} \simeq \sqrt{8\rho\xi_c^3/\sigma}(1 + 6\text{Oh}_{\xi_c})$ [46] and for viscoelastic liquids we can show that $t_{\text{pinch-off}} \simeq \sqrt{8\rho\xi_c^3/\sigma} + (3/2)\tau_E$ [31,66] where $(3/2)\tau_E$ is the inverse of the characteristic elongation rate $\dot{\epsilon} = -2/3\tau_E$ for a filament undergoing elasto-capillary thinning [66]. Substituting these into Eqs. (18) and (19), we arrive at the following general expression:

$$\frac{\langle d \rangle_m}{\langle d \rangle_s} \simeq \sqrt{2 + 3\chi/\sqrt{2}}, \tag{20}$$

where $\chi = \text{Oh}_{\xi_c} = \eta/\sqrt{\rho\xi_c\sigma}$ for Newtonian liquids of increasing viscosity and for viscoelastic solutions $\chi = \text{De}_{\xi_c} = \tau_E/4\sqrt{\rho\xi_c^3\sigma}$. In each of these expressions ξ_c is the critical thickness of the spiral ligament at which the primary breakup process initiates and can be found using Eq. (15).

For the PEO solutions, the test fluids approach the limit of a very dilute polymer solution, which means that the values of shear viscosity and Oh_R do not change and are very close to the corresponding values for the Newtonian solvent. However, due to the nonlinear viscoelastic effects induced in elongational flows, the extensional relaxation time (τ_E) and consequently De_R vary significantly for these PEO solutions. Measured values of $\langle d \rangle_m / \langle d \rangle_s$ are plotted for both viscous Newtonian (blue squares) and viscoelastic (red circles) in Fig. 20. It is evident that both viscoelastic and viscous effects tend to increase the ratio of the main to satellite droplet diameter. Predictions of our toy model [Eq. (20)] are also shown by the solid line. The good agreement between this simple scaling model and the corresponding measurements shows that both viscous retardation and the presence of an enhanced elongational viscosity resulting from fluid elasticity have similar effects on the average size of the satellite droplets. Meanwhile, our simultaneous measurements of droplet size distributions clearly show that while viscous retardation in the thinning process leads to very narrow size distributions for the secondary fragmentation process [e.g., $n_s \simeq 17$ for the 50 cSt silicone oil

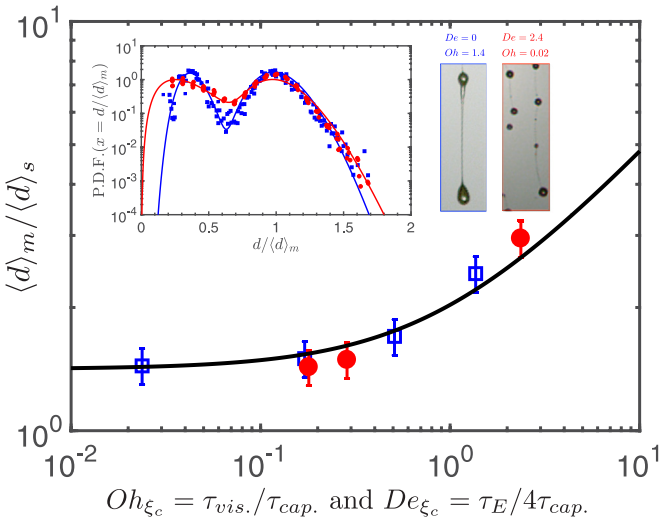

FIG. 20. Evolution in the ratio of the mean size of the main droplet to the satellite droplet: the abscissa shows the local Ohnesorge number of the filament $\mathrm{Oh}_\xi = \eta/\sqrt{\rho\xi_c\sigma}$ for different Newtonian test liquids (□) and the local Deborah number $\mathrm{De}_\xi = \tau_E/4\sqrt{\rho\xi_c^3/\sigma}$ for three viscoelastic fluids (●). The value of ξ is chosen based on the measured values of average droplet diameters ($\xi_c \simeq 66\ \mu$m) for these atomization conditions. The solid black line is the prediction of the simple toy model, described in Eq. (20). Inset images show the difference in terms of both size distributions and filament geometry for the most viscous silicone oil, $\mathrm{De} = 0$, $\mathrm{Oh} = 1.4$ (shown in blue) and the most elastic viscoelastic PEO solutions, $\mathrm{De}_{\xi_c} = 2.5$, $\mathrm{Oh}_{\xi_c} = 0.02$ (shown in red).

in Fig. 15(d)], the corresponding distributions for viscoelastic solutions are much broader ($n_s \simeq 4$ for the PEO 1M M_w 0.01% wt. solution). This viscoelastic broadening can be explained by the increase in the initial geometrical corrugations on the elongated filament that eventually break to form the secondary drops, due to nonlinear effects of viscoelasticity (see related discussions in Keshavarz *et al.* [33]).

IX. CONCLUSIONS

We have studied the fragmentation process in rotary atomization for both Newtonian fluids and dilute polymer solutions. Our results suggest that operating these atomizers in the ligament formation regime can have pronounced benefits over other types of atomizers. Organized and evenly spaced spiral ligaments, with shapes given by the involute of a circle, stretch and break in a repeatable manner. Consequently, the final droplet size distributions are relatively narrow and can be directly controlled by varying the rotation rate of the cup and the feed rate of the fluid. We have provided simple physical analyses for the different mechanisms that are involved in this fragmentation process and have derived analytical expressions for the number of ligaments, the extensional kinematics of individual fluid elements as they form the spiral ligaments and most importantly the variation in average droplet diameters with rotation rate and feed rate. Each of the predictions were compared and validated with results from a range of atomization experiments performed with both Newtonian and weakly viscoelastic liquids. However, certain aspects of the role of viscosity on the average droplet size at higher Ohnesorge numbers require further study, with additional focus on the dynamic effects of viscosity on the growth rate of instabilities involved in this rotary atomization process (such as ligament thinning). Understanding these effects may be particularly important for industrial applications where highly viscous Newtonian or complex liquids are used.

The measured droplet size distributions clearly show a bimodal behavior in the ligament formation regime. We show that the nature of this bimodal behavior is due to the existence of a secondary fragmentation process superimposed on the primary process. The main drop diameter $\langle d \rangle_m$ and the primary fragmentation in the ligaments is controlled by the linear instability of the continuously stretching spiral ligaments, and remains largely unaffected by the incorporation of fluid viscoelasticity due to the large length scales, and small amounts of total strain accumulated at this point in the process. However, the secondary fragmentation process that leads to the formation of satellite droplets occurs on the thin, highly stretched filaments which interconnect the main drops. Both viscous retardation and the enhanced elongational resistance increase the lifetime of these thin filaments, and when these thinner filaments finally break, they result in smaller mean satellite droplet sizes $\langle d \rangle_s$. A simple scaling model captured the dependence of $\langle d \rangle_s / \langle d \rangle_m$ on the local Ohnesorge number and Deborah number of the thinning filament. Finally, we note that the nonlinear elongational resistance of dissolved polymeric constituents in the fluid make the local topography of the thinning viscoelastic filaments more corrugated than the corresponding purely viscous secondary filament. This leads to much lower values of the parameter ($n_s \simeq 4$) in the corresponding Γ distributions for the secondary satellite droplets [67].

ACKNOWLEDGMENTS

B.K. and G.H.M. thank Axalta Coating Systems for their financial support. B.K. and G.H.M. also thank E. Villermaux for sharing his insightful ideas on the fragmentation process via personal communications. B.K. also thanks B. Eral and MIT central machine shop for help with fabrication of the atomizer and G. Dasin and W. H. Bowman from Axalta Coating Systems for help with measurements with industrial samples.

[1] A. K. Dickerson, Z. G. Mills, and D. L. Hu, Wet mammals shake at tuned frequencies to dry, J. R. Soc., Interface **9**, 3208 (2012).
[2] C. Davidson, *Shake* (Harper Design, New York, 2013).
[3] B. Andersson, Modeling and simulation of rotary bell spray atomizers in automotive paint shops, Ph.D. thesis, Chalmers University of Technology, 2013.
[4] P. Bär, Ueber die physikalischen Grundlagen der Zerstäubungstrocknung, Ph.D thesis, TH Karlsruhe, 1935.
[5] J. Domnick, Effect of bell geometry in high-speed rotary bell atomization, in *Proceedings of the 23rd annual conference on liquid atomization and spray systems, Brno, Czech* (2010), pp. 6–8.
[6] J. Domnick, High-speed rotary bell atomization of Newtonian and non-Newtonian fluids, in *12th International Conference on Liquid Atomization and Spray Systems, Heidelberg, Germany* (2012), pp. 2–6.
[7] S. Ogasawara, M. Daikoku, M. Shirota, T. Inamura, Y. Saito, K. Yasumura, M. Shoji, H. Aoki, and T. Miura, Liquid atomization using a rotary bell cup atomizer, J. Fluid Sci. Technol. **5**, 464 (2010).
[8] J. O. Hinze and H. Milborn, Atomization of liquids by means of a rotating cup, J. Appl. Mech.-Trans. ASME **17**, 145 (1950).
[9] R. P. Fraser, N. Dombrowski, and J. H. Routley, The production of uniform liquid sheets from spinning cups, Chem. Eng. Sci. **18**, 315 (1963).
[10] R. P. Fraser, N. Dombrowski, and J. H. Routley, The filming of liquids by spinning cups, Chem. Eng. Sci. **18**, 323 (1963).
[11] N. Dombrowski and T. L. Lloyd, Atomisation of liquids by spinning cups, Chem. Eng. J. **8**, 63 (1974).
[12] G. H. Gessinger and M. J. Bomford, Powder metallurgy of superalloys, Int. Metall. Rev. **19**, 51 (1974).
[13] S. J. Lukasiewicz, Spray-drying ceramic powder, J. Am. Ceram. Soc. **72**, 617 (1989).
[14] C. S. Parkin and H. A. Siddiqui, Measurement of drop spectra from rotary cage aerial atomizers, Crop Protect. **9**, 33 (1990).

[15] H. Jones and M. H. Burden, A rotary atomization technique for bulk splat cooling, J. Phys. E **4**, 671 (1971).
[16] H. Jones, Cooling, freezing and substrate impact of droplets formed by rotary atomization, J. Phys. D: Appl. Phys. **4**, 1657 (1971).
[17] S. Kazama, Steady-state paint flow under high centrifugal force: Atomization in spray painting, JSAE Rev. **24**, 489 (2003).
[18] K. R. J. Ellwood and J. Braslaw, A finite-element model for an electrostatic bell sprayer, J. Electrost. **45**, 1–23 (1998).
[19] J. R. Moore, Automotive paint application, *Protective Coatings* (Springer, Berlin, 2017), pp. 465–496.
[20] E. J. Hinch, Uncoiling a polymer molecule in a strong extensional flow, J. Non-Newtonian Fluid Mech. **54**, 209 (1994).
[21] T. Kamiya and A. Kayano, On the ligament type disintegration by the rotating disk atomizer, Chem. Eng. **34**, 287 (1970).
[22] P. Eisenklam, On ligament formation from spinning discs and cups, Chem. Eng. Sci. **19**, 693 (1964).
[23] T. Kamiya and A. Kayano, Film-type disintegration by rotating disk, J. Chem. Eng. Jpn. **5**, 174 (1972).
[24] K. R. Langley, D. Maynes, and T. T. Truscott, Eggs and milk: Spinning spheres partially immersed in a liquid bath, Phys. Fluids **27**, 032102 (2015).
[25] H. Hege, Flüssigkeitsauflösung durch Schleuderscheiben, Chemie Ingenieur Technik **36**, 52 (1964).
[26] Y. Oyama, M. Eguti, and K. Endou, Studies on the atomization of water droplets, Chem. Eng. **17**, 269 (1953).
[27] D. J. Ryley, Analysis of a polydisperse aqueous spray from a high-speed spinning disk atomizer, Br. J. Appl. Phys. **10**, 180 (1959).
[28] M. Ahmed and M. S. Youssef, Characteristics of mean droplet size produced by spinning disk atomizers, J. Fluids Eng. **134**, 71103 (2012).
[29] H. Sun, G. Chen, L. Wang, and F. Wang, Ligament and droplet generation by oil film on a rotating disk, Int. J. Aerospace Eng. **2015**, 769862 (2015).
[30] C. J. S. Petrie, Extensional viscosity: A critical discussion, J. Non-Newtonian Fluid Mech. **137**, 15 (2006).
[31] B. Keshavarz, V. Sharma, E. C. Houze, M. R. Koerner, J. R. Moore, P. M. Cotts, P. Threlfall-Holmes, and G. H. McKinley, Studying the effects of elongational properties on atomization of weakly viscoelastic solutions using Rayleigh Ohnesorge Jetting Extensional Rheometry (ROJER), J. Non-Newtonian Fluid Mech. **222**, 171 (2015).
[32] G. H. McKinley and M. Renardy, Wolfgang von Ohnesorge, Phys. Fluids **23**, 127101 (2011).
[33] B. Keshavarz, E. C. Houze, J. R. Moore, M. R. Koerner, and G. H. McKinley, Ligament Mediated Fragmentation of Viscoelastic Liquids, Phys. Rev. Lett. **117**, 154502 (2016).
[34] Lord Rayleigh, Investigation of the character of the equilibrium of an incompressible heavy fluid of variable density, Proc. London Math. Soc. **s1-14**, 170 (1882).
[35] G. I. Taylor, The instability of liquid surfaces when accelerated in a direction perpendicular to their planes, in *Proceedings of the Royal Society of London A: Mathematical, Physical and Engineering Sciences*, Vol. 201 (The Royal Society, London, 1950), pp. 192–196.
[36] S. Chandrasekhar, *Hydrodynamic and Hydromagnetic Stability* (Dover Publications, Oxford, 1961).
[37] NCFMF, *Illustrated Experiments in Fluid Mechanics: The NCFMF Book of Film Notes* (MIT Press, Cambridge, MA, 1972).
[38] M. S. Plesset and C. G. Whipple, Viscous effects in Rayleigh-Taylor instability, Phys. Fluids **17**, 1 (1974).
[39] Later on, we will relax this assumption.
[40] C. Huygens, *Horologium oscillatorium sive de motu pendulorum ad horologia aptato demonstrationes geometricae* (Parisiis, 1673).
[41] J. G. Yoder, Christiaan Huygens, book on the pendulum clock (1673), in *Landmark Writings in Western Mathematics 1640-1940* (Elsevier Science, 2005), pp. 33–45.
[42] F. C. Moon, *The Machines of Leonardo Da Vinci and Franz Reuleaux: Kinematics of Machines from the Renaissance to the 20th Century*, Vol. 2 (Springer Science & Business Media, Berlin, 2007).
[43] After personal communication with E. Villermaux, we found out that a similar geometry is observed in the study of bursting bubbles [59,68,69].

[44] T. Kamiya, An analysis of the ligament-type disintegration of thin liquid film at the edge of a rotating disk, J. Chem. Eng. Jpn. **5**, 391 (1972).
[45] In other words $t' = 0$ is a virtual moment that never happened and the minimum value of t' for every fluid element is $t'_{\min} = e/\omega$ which correspond to the time at which the element leaves the edge of the actual cup $r = R$.
[46] J. Eggers and E. Villermaux, Physics of liquid jets, Rep. Prog. Phys. **71**, (2008).
[47] R. Krechetnikov and G. M. Homsy, Crown-forming instability phenomena in the drop splash problem, J. Colloid Interface Sci. **331**, 555 (2009).
[48] L. V. Zhang, P. Brunet, J. Eggers, and R. D. Deegan, Wavelength selection in the crown splash, Phys. Fluids **22**, 122105 (2010).
[49] P. Marmottant and E. Villermaux, Fragmentation of stretched liquid ligaments, Phys. Fluids **16**, 2732 (2004).
[50] E. Villermaux, V. Pistre, and H. Lhuissier, The viscous Savart sheet, J. Fluid Mech. **730**, 607 (2013).
[51] S. Le Dizès and E. Villermaux, Capillary jet breakup by noise amplification, J. Fluid Mech. **810**, 281 (2017).
[52] V. F. Dunskii and N. V. Nikitin, The size of "secondary" droplets when a liquid is atomized by a rotating disk, J. Eng. Phys. **17**, 791 (1969).
[53] P. Marmottant and E. Villermaux, On spray formation, J. Fluid Mech. **498**, 73 (2004).
[54] S. Kooij, R. Sijs, M. M. Denn, E. Villermaux, and D. Bonn, What Determines the Drop Size in Sprays? Phys. Rev. X **8**, 031019 (2018).
[55] E. Villermaux, Fragmentation, Annu. Rev. Fluid Mech. **39**, 419 (2007).
[56] J. C. Ogbonna, M. Matsumura, T. Yamagata, H. Sakuma, and H. Kataoka, Production of micro-gel beads by a rotating disk atomizer, J. Ferment. Bioeng. **68**, 40 (1989).
[57] L. M. Boize and N. Dombrowski, The atomization characteristics of a spinning disk ultra-low volume applicator, J. Agric. Eng. Res. **21**, 87 (1976).
[58] T. Kamiya and A. Kayano, Disintegration of viscous fluid in the ligament state purged from a rotating disk, J. Chem. Eng. Jpn. **4**, 364 (1971).
[59] H. Lhuissier and E. Villermaux, Bursting bubble aerosols, J. Fluid Mech. **696**, 5 (2011).
[60] E. Villermaux, P. Marmottant, and J. Duplat, Ligament-Mediated Spray Formation, Phys. Rev. Lett. **92**, 074501 (2004).
[61] E. Villermaux and B. Bossa, Single-drop fragmentation determines size distribution of raindrops, Nat. Phys. **5**, 697 (2009).
[62] E. Villermaux and B. Bossa, Drop fragmentation on impact, J. Fluid Mech. **668**, 412 (2011).
[63] A. Vledouts, N. Vandenberghe, and E. Villermaux, Fragmentation as an aggregation process: The role of defects, Proc. R. Soc. London A **472**, 2185 (2016).
[64] A. Vledouts, J. Quinard, N. Vandenberghe, and E. Villermaux, Explosive fragmentation of liquid shells, J. Fluid Mech. **788**, 246 (2016).
[65] S. Middleman, Stability of a viscoelastic jet, Chem. Eng. Sci. **20**, 1037 (1965).
[66] G. H. McKinley, Visco-elasto-capillary thinning and breakup of complex fluids, in *The Annual Rheology Review* (The British Society of Rheology, Aberystwyth UK, 2005), pp. 1–48.
[67] B. Keshavarz, Nonlinear dynamics of complex fluids in fragmentation and fracture, Ph.D. thesis, MIT, 2017.
[68] H. Lhuissier and E. Villermaux, Soap Films Burst Like Flapping Flags, Phys. Rev. Lett. **103**, 054501 (2009).
[69] H. Lhuissier and E. Villermaux, Bursting bubbles, Phys. Fluids **21**, 091111 (2009).